



ASHESI UNIVERSITY

DESIGN AND FABRICATION OF A MODULARIZED HUMANOID

ARM WITH PNEUMATIC ARTIFICIAL MUSCLES

CAPSTONE PROJECT

B.Sc. Mechanical Engineering

Ronny Paa Kwesi Panford

2021

ASHESI UNIVERSITY

**DESIGN AND FABRICATION OF A MODULARIZED HUMANOID
ARM WITH PNEUMATIC ARTIFICIAL MUSCLES**

CAPSTONE PROJECT

Capstone Project submitted to the Department of Engineering, Ashesi
University in partial fulfilment of the requirements for the award of Bachelor of
Science degree in Mechanical Engineering.

Ronny Panford

2021

DECLARATION

I hereby declare that this capstone is the result of my own original work and that no part of it has been presented for another degree in this university or elsewhere.

Candidate's Signature:



Candidate's Name:

Ronny Paa Kwesi Panford

Date:

27/04/2021

I hereby declare that preparation and presentation of this capstone were supervised in accordance with the guidelines on supervision of capstone laid down by Ashesi University College.

Supervisor's Signature:

.....:

Supervisor's Name:

Dr. Stephen Armah

Date:

.....:

Acknowledgements

To my supervisor, Dr. Stephen Armah, whose patience, encouragement and academic advice helped me undertake this project. His particular expertise in control and mechanical engineering guided my design considerations across the systems to be implemented under this project.

I would like to acknowledge Dr. Heather Beem, for her timely and selfless guidance and knowledge contributions to this project. Her thought-provoking assessments and queries into the application of the system designs and practicality, drove an iterative process to find efficient solutions and redefine the project scope.

A special thanks extended to all lecturers of Ashesi University's Mechanical Engineering Department, for the broad contributions to this project through their feedbacks. I would particularly like to acknowledge the dedication and patience of my parents, Mr. Victor A. Panford and Mrs. Marie-Antoinette Panford, throughout this project. Without their aid in mobilizing resources and facilitating the fabrication of the project designs, this project would not have made considerable strides.

I appreciate the consistent support of my course mates of the class of 2021, with notable mentions being Julianne Djan-Sampson, Lloyd Teta, Joe Nii Armarteifio, Oluwatobiloba Omole, Ivana Barley, and Oheneba Aggrey. I give immense thanks to Diana Evans, as well as acknowledge Opanin Kwadwo Akuffo, Adobea Dampare-Addo, Nana-Araba Aidoo and all other friends and family for keeping me grounded and motivated throughout the different stages of this project.

Finally, above all things, I give all thanks and praise to God, for it has been by His will, His grace, and His mercies this project has come to fruition.

Abstract

With increase investment in the development of humanoids, there offers a window of opportunity to leverage the rapidly growing market of soft robotics in our strides towards more accurate biomimetic motion and study of humanoids and their applicatory areas.

This project encompasses the systematic design, implementation and testing of a lightweight low-cost humanoid arm that utilizes Pneumatic Artificial Muscles (PAM). These muscles do not only exhibit twistable and bendable human-like muscle contractions but modularized in design to stand as a complete controllable unit which may be dissociated and mountable on a support frame on its own.

This project achieves the design of a mobile arm unit with total weight of less than 2kg of which is distributed with one-third the weight being borne on the arm. The realized power-to-weight ratio of near 5W per kilogram, under an approximate 13.5 litre per minute rate of pressurization is of desired muscle force, and flex speeds. The McKibben tubing choice of PAM is experimentally validated under a linear fit for its force-contraction performance.

This design makes considerable strides in cutting down weight, leveraging power, and being much cheaper than existing solutions. Comparable lightweight arm designs of which some are commercially available have weights of 38kg (Mitsubishi PA10arm), 14kg (KUKA lightweight arm), etc., with power-to-weight ratios of near 1W/kg. However, this project designs cuts down these weights drastically to about 2kg (without any sensory unit yet) and more than doubles the power to weight ratios mentioned.

Table of Content

DECLARATION.....	I
Acknowledgements	II
Abstract.....	III
Table of Content.....	IV
List of Tables	VIII
List of Figures.....	X
List of Abbreviations	XIII
Chapter 1: Introduction	1
1.1 Background	1
1.2 Problem Statement	3
1.3 Requirements.....	4
1.3.1 Functional Requirements	4
1.3.2 Design Requirements	4
1.4 Design Specifications	5
1.5 Objectives.....	6
1.6 Scope	6
1.7 Proposed Solution	7
Chapter 2: Literature Review and Related Work.....	9
2.1 Literature Review.....	9
2.1.1 The humanoid arm history and musculoskeletal system mapping.....	9
2.1.2 Soft McKibben-based actuators using traditional pumps	9
2.1.3 Positional sensing and control systems for pneumatic actuation	10
2.1.4 Control systems for pneumatic actuation.....	12

2.2 Related Work.....	13
2.2.1 Alternative soft-robotic arm actuation using non-traditional pumps	13
2.2.2 Possibility for higher power agile soft actuators.....	14
Chapter 3: Design & Methodology	16
3.1 Design Derivation and Constraints	16
3.2 Humanoid arm performance evaluation criteria.....	19
3.3 Conceptual Designs and Selection	20
3.3.1 Skeletal framework/chassis preliminary designs	20
3.3.2 Design A	21
3.3.3 Design B.....	22
3.3.4 Design C.....	24
3.3.5 Skeletal framework selected design	27
3.4 Key Component Selection.....	28
3.4.1 Valve system configuration	28
3.4.2 Soft actuator system configuration.....	29
3.4.3 Limb primary material selection	29
3.4.4 Limb joint material selection	30
3.5 Modelling the Arm's Mechanical Operation	31
3.5.1 Operational loading scenarios.....	31
3.5.2 Identifying loading cases for highest stresses at joints/limbs	33
3.6 McKibben Muscle Design and Sizing.....	34
3.6.1 Muscle loading and extensions for wrist flexion/extension.....	35
3.6.2 Muscle loading and extensions for elbow flexion/extension	36
3.6.3 Muscle loading and extensions for shoulder rotation	36
3.6.4 Muscle loading and extensions for shoulder flexion/extension	37
3.6.5 Muscle loading and extensions for shoulder abduction/adduction	38
3.7.6 Summary of Muscle load operations.....	39
3.7 Determining required muscle performance.....	40
Chapter 4: Analysis	42
4.1 Analytical Analysis	42
4.1.1 Analysis of Load Case 1A	43
4.1.2 Analysis of Load Case 1B.....	45
4.1.3 Analysis of Load Case 2B.....	47

4.1.4 Analysis of Load Case 3C.....	48
4.1.5 Analysis of Load Case 4B.....	50
4.1.6 Analysis of Load Case 4D	52
4.1.7 Analysis of Load Case 5E.....	54
4.2 Numerical Analysis	55
4.2.1 Identified key stress components	55
4.2.2 Stress analysis of shoulder rod under Operational Load Scenario 3C	56
4.2.3 Stress analysis of shoulder socket rod under Load Scenario 3C, 4D & 5E	57
4.2.4 Stress analysis of shoulder under all Operational Load Scenario	59
4.2.5 Stress analysis of wrist under Bending and Axial Operational Load Scenarios	63
4.2.6 Stress analysis of shoulder socket under Operational Load Scenario 1C & 3C.....	64
4.2.7 Stress analysis of double cardan joint under Operational Load Scenario 3C	65
4.3 Muscle Fabrication and Experimental Analysis.....	66
Chapter 5: Implementation.....	70
5.1 Skeletal structure fabrication.....	70
5.1.1 Arm fabrication.....	70
5.1.2 Resulting arm assembly	72
5.1.3 Resulting shoulder assembly.....	73
5.2 Muscle assembly	74
5.3 Complete musculoskeletal assembly.....	75
5.4 Pressure control schematic and implementation of pump system.....	77
5.4 Arm power performance testing.....	79
Chapter 6: Results and Discussions	80
6.1 Results	80
6.1.1 Mechanical design results summary	80
6.1.2 Actuation performance results summary	81
6.2 Discussions.....	82
Chapter 7: Conclusion and Future Work	84
7.1 Conclusion.....	84
7.2 Future Work	85
7.2.1 Proposed Control System.....	85
7.2.2 Muscle Optimization.....	86

7.2.3 Joint improvements for mechanical advantage 87

References 88

Appendix 93

Appendix A 93

Appendix B 94

Appendix C 95

Appendix D 96

Appendix E 97

Appendix F 98

Appendix G 99

List of Tables

Table 3.1: Joint determination and degrees of motion for humanoid arm.....	19
Table 3.2: Evaluation criteria.....	19
Table 3.3: Pugh chart for valve system selection	28
Table 3.4: Pugh chart for soft actuator system selection	29
Table 3.5: Pugh chart for limb material selection	30
Table 3.6: Pugh chart for limb joint material selection	30
Table 3.7: Arm extreme orientations and loading effects	32
Table 3.8: Arm load case comparison for maximum loading effects	33
Table 3.9: Calculated wrist joint muscle flexion/extension properties.....	36
Table 3.10: Calculated elbow joint muscle flexion/extension properties	36
Table 3.11: Calculated shoulder joint muscle rotational drive properties	37
Table 3.12: Calculated shoulder joint muscle flexion/extension properties	38
Table 3.13: Calculated shoulder joint muscle abduction/adduction properties	38
Table 3.14: Summary of paired muscles' maximum force and contractions	39
Table 3.15: Muscle dimensions	41
Table 3.16: Muscles maximum operational pressures.....	41
Table 4.1: Static/Yield analysis of forearm-elbow section in load case 1A.....	43
Table 4.2: Fatigue analysis of forearm-elbow section in load case 1A	44
Table 4.3: Static/Yield analysis of upper limb fixed point in load case 1B.....	45
Table 4.4: Fatigue analysis of upper limb fixed point in load case 1B	46
Table 4.5: Static/Yield analysis of upper limb in load case 2B	47
Table 4.6: Fatigue analysis of upper limb in load case 2B	48
Table 4.7: Static/Yield analysis of shoulder socket rod in load case 3C	49
Table 4.8: Fatigue analysis of shoulder socket rod in load case 3C	50

Table 4.9: Static/Yield analysis of upper-elbow joint in load case 4B.....	51
Table 4.10: Fatigue analysis of shoulder socket rod in load case 4D	52
Table 4.11: Fatigue analysis of shoulder socket rod in load case 4D	53
Table 4.12: Static/Yield analysis of lower-elbow joint in load case 5E	54
Table 4.13: Shoulder pulley rod bearing muscle force results	56
Table 4.14: Shoulder pulley rod torsional results	57
Table 4.15: Shoulder socket rod bearing arm load results.....	58
Table 4.16: Shoulder socket rod torsional results.....	59
Table 4.17: Shoulder vertically adducted bearing arm load results.....	60
Table 4.18: Shoulder horizontally abducted (elevated) bearing arm load results	61
Table 4.19: Shoulder horizontally flexed/extended bearing arm load results	62
Table 4.20: Wrist joint axially loaded results	63
Table 4.21: Wrist joint laterally loaded results.....	64
Table 4.22: Shoulder socket maximum torsional elevation results	65
Table 4.23: Double cardan shaft torsional results	66
Table 6.1: Critical mechanical analysis results for primary parts	80
Table 6.2: Overall arm mechanical properties.....	81
Table 6.3: Arm operational performance.....	81
Table B.1: Moving mass and torque at joints	94
Table C.1 Small Muscle Experimental Load-Contraction Data at 50 kPa	95
Table C.2 Small Muscle Theoretical Load-Contraction Data at 50 kPa.....	95
Table C.3 Large Muscle Experimental Load-Contraction Data at 50kPa	95
Table C.4 Large Muscle Theoretical Load-Contraction Data at 50 kPa.....	95

List of Figures

Figure 3.1: (a) Anatomy of arm, (b) Joint mapping for degrees of freedom	16
Figure 3.2: (a) Wrist joint architecture, (b) Normalized workspace angles.....	18
Figure 3.3: Conceptual design sketches.....	20
Figure 3.4: Overview of conceptual design A	21
Figure 3.5: CAD model of conceptual design A.....	22
Figure 3.6: Overview of conceptual design B	23
Figure 3.7: CAD model of conceptual design B.....	23
Figure 3.8: Arm mobility and muscle limitations in design B.....	24
Figure 3.9: Overview of conceptual design C	25
Figure 3.10: CAD model of conceptual design C.....	26
Figure 3.11: CAD model perspectives of final design.....	26
Figure 3.12: Forearm muscles FBD analysis for wrist joint flexion/extension.....	35
Figure 3.13: Upper arm muscles FBD analysis for elbow joint flexion/extension.....	36
Figure 3.14: Upper arm muscles FBD analysis for upper arm shoulder rotation	37
Figure 3.15: Shoulder muscles FBD analysis for shoulder joint flexion/extension	37
Figure 3.16: Shoulder muscles FBD analysis for shoulder joint abduction/adduction.....	38
Figure 3.17: McKibben tubing overview.....	39
Figure 4.1: FBD and load analysis of forearm-elbow section in load case 1A	43
Figure 4.2: FBD and load analysis of full arm length in load case 1B	45
Figure 4.3: FBD and load analysis of applied upper-arm torque in load case 2B	47
Figure 4.4: FBD and load analysis of applied shoulder torque in load case 3C	49
Figure 4.5: FBD and load analysis of upper-elbow joint in load case 4B	51
Figure 4.6: FBD and load analysis of shoulder in load case 4D.....	52
Figure 4.7: FBD and load analysis of lower-elbow joint in load case 5E	54

Figure 4.8: F.O.S contour results for loaded shoulder rod at shoulder pulley unit	56
Figure 4.9: F.O.S result for torsional stress in shoulder rod at shoulder pulley unit	57
Figure 4.10: Simulation results for shoulder socket rod under bending load	58
Figure 4.11: F.O.S result for torsional stress in shoulder socket rod	59
Figure 4.12: Simulation results for shoulder as connecting upper arm is axially loaded	60
Figure 4.13: Simulation results for shoulder as upper arm is horizontally abducted	61
Figure 4.14: Simulation results for shoulder as shoulder is in horizontal extension	62
Figure 4.15: Simulation results for wrist joint as wrist receptor is axially loaded	63
Figure 4.16: Simulation results for wrist joint as wrist receptor is laterally loaded	64
Figure 4.17: Simulation results for shoulder socket as shoulder rod at maximum bending	64
Figure 4.18: Simulation results for components of double cardan joint during torsion	66
Figure 4.19: Fabrication of McKibben muscles	67
Figure 4.20: Plot of small muscle load-contraction under 50 kPa test pressure	68
Figure 4.20: Plot of large muscle load-contraction under 50 kPa test pressure	69
Figure 5.1: 3D-printed lightweight arm joint components	70
Figure 5.2: Sheet metal cutting of humanoid arm shoulder support and limbs	71
Figure 5.3: Bearing housed in stainless steel metal strips adhered with epoxy steel	71
Figure 5.4: Fabrication of cross-linkage for connecting the double cardan joint yokes	72
Figure 5.5: Fully jointed arm skeletal unit	72
Figure 5.6: Assembled shoulder module top view with shoulder tilted in extension	73
Figure 5.7: Assembled shoulder module side view with shoulder in abduction	73
Figure 5.8: A muscle connection to joint pulley system (forearm wrist joint example)	74
Figure 5.9: Complete modularized arm with muscle and auxiliary units connected	76
Figure 5.10: Full musculoskeletal system of humanoid arm with labelled parts	77
Figure 5.11: Schematic of proposed pressure control valve and pump system	78

Figure 7.1: Proposed humanoid arm control system flow chart	86
Figure A.1: S-N generated curve for ABS material	93
Figure D.1: Specifications for Sub-miniature pilot 5/3-way solenoid valve	96
Figure E.1: Specifications for Wattmizer Proportional 2 Way Normally Closed Valves	97
Figure F.1: Datasheet for the Airpo D2028B Miniature-Pressure Pumps	98
Figure G.1: Assembly drawing	98

List of Abbreviations

3D – Three-dimensional

AI – Artificial Intelligence

CAD – Computer Aided Design

CNC – Computer Numerical Control

D.O.F – Degree(s) of freedom

FBD – Free Body Diagram

F.O.S – Factor of Safety

MC – Microcontroller

PAM – Pneumatic Artificial Muscles

UHMWPE – Ultra-high molecular weight polyethylene

Chapter 1: Introduction

This chapter explores the problem intended to be designed for and how it informs the project scope, intended design solution and constraints based on the leveraged benefits and sphere of opportunity soft robotics offers.

1.1 Background

With heightened interests in the area of artificial intelligence, the field of robotics has neared centre stage in leveraging improved safety, assistive healthcare, and most especially scalable and accelerated manufacturing. Radical advancements in the very new field of soft robotics, are quickly driving robotic limb-joint actuation towards more fluid natural-like motion, of which are better adaptive to unstructured environments, and much realistically capably of achieving near-biological motion [1]. This opens the possibility of robotic implementation in much intricate tasks of which require smoother limb curls, and not only greater but faster motion precision. Succumbing the demerit of noise, backlash effect, and rigidity accustomed with geared motor systems [2], pneumatic actuators are a pressure-driven category of soft actuators with very high force intensities compared to 5 other soft actuation methods: light, heat, chemical, applied electric and magnetic responsive actuators [3]. Despite the development of artificial pneumatic muscles such as McKibben tubing, pressure-driven actuators are not only set-back by the requirement of external, typically heavy, pressure pumps, they also introduce a new non-linearity dimension to their motion of which require much complex models and algorithmic control [4].

A vast number of robots today perform human labor tasks most especially in the field of manufacturing, with the earliest dated robot, according to the Tech Museum of Innovation, producing ashtrays [5]. Robots have quite rapidly found their purpose in our world, due to reasons of heightened speed, multipliable strength, safety, and the drive to eliminate a majority

of human error. It however should be known that these innovations and boomed growth in the field has been largely dominated by European, Asian and American markets with increased investments in the field of humanoids [6]. It has only been recently that two African countries have hopped into the market stream for robotics, one being South Africa [7], with the others either lacking completely in the field or in very minute quantities, import these robotic systems at high costs and under foreign management into their industries and research institutions. There has been very little to no contribution to the booming market of robotics, especially the ever-explosive market of soft robotics. Humanoid robots offer us the ability to research into human musculoskeletal mechanical systems to mimic human-like motion, giving us insights into applicatory areas such as bio-medical assisted solutions and exoskeletal mechanical suits [8]. Such suits have increased mechanical use and proven performance in accelerating recovery of temporarily disabled persons as well as alleviating any motor disabilities faced by fully immobile persons [9].

Unfortunately, bringing the scope of Africa's underperformance in this field even more narrowly to Ghana, development of wholistic robots even at the barest minimum is undertaken as low budget and development projects. Typically, in occurring high-school and university competitions, or small-sized student trainings such as by Khalmax Robotics [10], of which are incapable of advancing into any stage of large-scale production. Ghana has had an extremely slow to stagnant progression into the field of humanoids and exoskeletal systems with one of the very few projects gaining publicity was a 25cm half assembled servo-powered prototyped miniature humanoid of which had no onboard central processor implemented yet, let alone the embedding of any AI to facilitate its autonomous operation [11]. Ghana and many countries are dramatically missing out in the beneficial advancements of robotics, most especially soft robotics ushered in by the increased shift towards bio-inspired robotics. These are by and large, taking center stage in developed countries and can be found in a vast number of fields even in

potential space exploration [12], not just in the field of manufacturing and defense anymore. Whereas underdeveloped countries especially in Africa remain stagnant in centuries behind research and development, mainly due to lack of interest, high cost, unavailability of such technologies domestically, and as such high importation cost, amongst other reasons [13].

By market report released in June 2020, by Mordor Intelligence and other notable market analyzers, as of 2019 the soft robotics market was globally valued at \$645.45 million and has one of the largest market growth with a 40% compound annual growth rate towards an expected \$4.965 billion market value by 2025, with North America holding a significant share of this valuation [14, 15]. There is a need for light weight, low cost, easily producible robotic technology paramount to Africa's accelerated growth into this market.

1.2 Problem Statement

The rigidity of modern-day robots which utilize dense steel and aluminum structures housing powerful but heavy motor units form a limitation in handling unstructured and complex environments and in modeling close bio-mechanical structures. Their large weight, demerit their use in ideally lighter mobile solutions such as humanoids requiring larger power inputs to control already heavily massed limbs. To date most robots, especially in the field of wearable robotics are based on this rigid uncomfortable motored motion, or fluidic actuators which unfortunately require external pumps or compressors, limiting feasibility in portable systems. Thus, despite the merits enabled by fluidic actuators, as opposed to electromagnetic motor control, there needs to be a lighter weight, internally integrated pneumatic system to leverage the benefits of soft actuation while eliminating its aforementioned limitation.

1.3 Requirements

1.3.1 Functional Requirements

- A humanoid arm that benefits from its human-like shape and scale for telemetric operation in otherwise, harmful remote locations requiring the use of humanoids.
- The arm must be accurate in its gestures and contribute to a holistically low-cost humanoid design.

1.3.2 Design Requirements

- The arm must be portable and attachable as a whole modularized replace unit on its own.
- Base of the humanoid arm must be mounted vertically as to represent the anthropometrically correct shoulder of the arm [16].
- The design must be able to incorporate different types of clasps/grippers/hands for different purposes.
- The design and used architecture must be upgradable/hackable compared to high-end commercially available robotic arms.
- The arm must be devoid of any tethering, be it externally fed-in tubing or wiring that is outside of the humanoid, to enable mobility, a compact design, and not restrict the operating radius to which the humanoid can move.
- The arm must be of weather-resistant material and all electrical units must be properly grounded and insulated to ensure there is no risk of electrocution during interaction with people and other living things.

1.4 Design Specifications

This section details system design specifications for the humanoid arm that are configuration and actuation independent. These specifications include required capabilities and constraints based on the design requirements presented.

- The arm must operate with an end effector reach within a workspace of radius at least 0.55m from its shoulder joint, to more correctly represent the full reach biomimetic motion of the adult male human arm [16].
- Low cost: the arm should cost no more than \$4000 as assessed against low-cost 3D-printed humanoid arms averaging \$11,500, of which REACHY is benchmarked as being a super low-cost solution within this price for a complete unit [17].
- Arm must ascertain operation under an estimated payload of 9kg on its end-effector, as the average human is physically guided by limiting their carrying limit to about 1/5 their body weight averaged at 40kg, which amounts to a summed 18kg load carry by both arms with minimal effort [18]. Thus, the arm must at least meet this load bearing capacity.
- Lightweight with an overall weight of less than 5.7kg as this is averagely the size of small unit humanoid arms thus achieving lower categorizes humanoid arms in a lighter weight class [17, 19].
- Have at least 5 degrees of freedom enabled with 3 joints.
- With the average operating time of humanoids being between 2-3 hours [20], with thousands of robots such as achieving this operation time. As such, the arm must perform for at least 4 hours without any considerable thermal or musculoskeletal failures.
- Low voltage and power requirements of the actuator system of which can be easily integrated into the electrical system of the humanoid of which typically is powered with

a maximum voltage of 24.9V and 26.7 – 30Wh battery unit as in the NAO programmable humanoid.

- Humanoid arm's actuators must be compact, small and housed within the arm and not externally.

1.5 Objectives

The main objective is to build a 5-DOF robotic arm, with an attached pneumatic artificial muscular system for actuation. Powered by onboard compact-sized electric high-pressure pumps, without the need for an externally situated pump or compressor.

The specific objectives are:

- Design, build, and test varied sized McKibben tubing for tailored pressure-extension performances required.
- Synchronize artificial muscular operation for smoother faster anthropoid operation.
- Calculate theoretical power-to-weight ratio of humanoid arm. Obtain an experimental value for the power-to-weight ratio. Decrease variation between theoretical calculation and realized performance.
- Perform finite element analysis of arm structure, to eliminate excess design material, without compromising strength, and assess design success.
- Model power output and flex speed to attain a minimum performance that matches or surpasses the average existing solutions within the arm design category.
- 3D print humanoid arm skeletal structure.

1.6 Scope

The project focuses on the design and development of a humanoid arm solely constrained to the upper arm to forearm anatomy. The modeling and development of pneumatic

muscular system for the hand, comprising of the palm and fingers are not included in this study. An interchangeable fixed end effector is assumed to substitute motor hand movement. Only the main motor functions and movement in these areas of the arm are targeted to mimeograph the limited degrees of freedoms per joint of the muscular anatomy of a typical human arm without heightened flexibility like a contortionist. Lastly, the actual movement of the shoulder is not included in the study, but the degrees of motion through the rotation of the upper arm in its socket (joint) is.

The humanoid arm is environmentally limited to operate within an obstacle-free space, under standard room temperature and pressures. The humanoid arm cannot be expected to be spatially recognize objects within its working radius, and maneuver around it, as the arm on its own, within this purpose of design is not equipped with its own sonar or visual sensors decoupled from the humanoid as a whole.

1.7 Proposed Solution

This project seeks to leverage the high power-to-weight ratio, smooth continuum motion and efficiency perks of pneumatic muscles while eliminating the mobility constraint due to the lack of on-boarding pressure pumps and external tubing. This is to be achieved by having compact, lightweight, vacuum to high pressure controllable micro-pressure pumps on-boarded and attached onto the skeletal framework of the humanoid arm. Utilizing such highly compact pumps increases the capability of decreasing total arm weight as these pumps are light weighted, of masses averaging 200g, yet capable of supplying output forces matching or exceeding counterpart motored actuation without gearing systems. A lower pump weight and dimension, consequently, would enable the design of less rigid and bulky motor mounts and gear boxes, decreasing non-strength contributing material usage in the skeletal frame.

With air (or atmospheric non-particulate gas) as the proposed pumping medium, this artificial pneumatic muscular system requires no additional fluid storage device or pre-pressurizer, giving it heightened agility and lower overall weight.

Lastly, such micro-pressure pumps would be of DC voltage supply with low voltage ratings, averagely below 30V, making their use in a humanoid arm highly suitable for integration with onboard PCB systems and low electronics power feeds and battery rating.

Chapter 2: Literature Review and Related Work

This chapter explores the existing works and modules pertaining to this projects design and purpose, through identifying standard design methodologies and architecture.

2.1 Literature Review

The universal standard methodology to humanoid design is studied for application in this project, and then dives into exploring research into the various modules of this project, from soft muscle actuation to control methodologies.

2.1.1 The humanoid arm history and musculoskeletal system mapping

“Humanoid robots are designed and built to mimic human form and movement.” [21]. As such, humanoid robots are designed to attain the typical size and physical abilities, to exhibit autonomous human-like work in our environments. The initial introduction of fully robotic systems were industrial manipulators of the 1960s, with functionality very limited to pre-programmed movements, up until 1960 in which interests in robots being more autonomous and complex after the introduction of microprocessors [22]. Moon, Ko and Bae discuss the universal standard methodology to design humanoids, more specifically a humanoid arm as example, to which would be the intended purpose of this project.

2.1.2 Soft McKibben-based actuators using traditional pumps

In an extremely extensive design and investigation of an efficient high performing pneumatic muscle and jointing system, a straight-fibre type artificial muscle has been developed, of which surpasses the output of the meshed sleeve McKibben-type. It produces as much as 1700N of force at a faster rate at just 0.54MPa internal pressure as opposed to a 580N output under the same pressure in a regular McKibben Muscle [23]. Two types of wrist joint

manipulator configurations were designed and built for the 7-degree-of-freedom (7-DOF) manipulator. The study concludes sufficiently on the use of a pulley-in-pulley type wrist joint as it has no gaps between the muscled flexion-extension axis and the ulnar-radius deviation axis, as compared to a designed universal joint-type wrist joint which causes interference in the driving force due to a necessary jointing [23]. This coupled with these straight-fiber artificial muscles ascertains high power output with minimal discontinuities due to the freely rotating yet load transferring pulley-in-pulley joints. Moreover, a proposed control system for this manipulator regarding the joint angle and stiffness, entailed a PI control method with MATLAB Simulink modelling and regulating the joint angle using a torque feedback control method, of which inspects the joint stiffness.

The design pitfalls are still the use of an external compressor and high weight of joints in excess of 5kg.

2.1.3 Positional sensing and control systems for pneumatic actuation

As much as the performance of a humanoid arm is highly dependent on its power output through its actuators, it is also equally dependent on the onboard force and displacement sensors to make sure the adequate power is being outputted on the required trajectory is being accurately followed. Traditional geared motor robots tend to measure the current draw of the motors during operation to assess torque demand by the motor and in turn force output, although this process requires no additional sensing unit, it has a plethora of problems. The problems span low bandwidth, large inaccuracies and exceeding noise in current readings due to even interference from the motor itself during operation and heating.

As such, higher precision robots lean towards torque sensor / torquemeters. Rotary encoders are transducers that are designed to measure the rotation of a mechanical component (shaft, axle, etc.) and send a digital signal to the control system [24]. The initial go-to standard

for rotary encoders were based on optical measurement techniques, of which comprise of a 'code disk' having concentric pattern of transparent and opaque areas the slow light through onto a photocell during rotation, generating a means for depicting the absolute rotational angle from this pattern [25]. However, these are expensive, requiring larger sizes for better accuracy. They are also unfavorably prone errors due to humidity and vibrational loading.

In substitution, Magnetic encoders, utilizing hall-effect sensors are more compact, less susceptible to dust and moisture and more tolerant of shock loads, making them a probable component for this project. By combining the output of several Hall-effect sensors through sophisticated signal processing algorithms, an accuracy and highly sufficient resolution of 17-bits is attainable as manufactured in torque and rotary sensors by POSITAL-FRABA. Assessing contribution to control performance, they provide very little feedback noise suitable for closed loop control of high-speed dynamic control systems [26].

With respect to soft actuation, a vast majority of sensing use the principle of strain gauges and more directly record the output linear displacement of the actuator itself, as opposed to the joint rotation. A notable novel study for the case of Pneumatic Artificial Muscles, tested out in this with McKibben actuators, is to have the meshing of the muscle itself measure its contraction length and force output.

The method makes the braid of these fiber-reinforced actuators, out of insulated wires that form an electric circuit. Changes in the inductance and resistance of this circuit can be related to muscle contraction length and muscle force, of which was validated experimentally. The realization of this method was done with two McKibben muscles that were evaluated under a variety of air pressures (0-200 kPa) and loads (0-45 N). The experiments confirmed a theoretical prediction of a roughly linear relationship between the measured inductance and the contraction length, as well as a strong correlation between the measured resistance and the actuator force [27]. This method capable of determining force with a resolution of 5N and

contraction length with a resolution of 0.5 mm [27]. This technique can be used to create flexible, precise, and robust self-sensing actuators that benefit a multitude of robotic applications.

2.1.4 Control systems for pneumatic actuation

A closed-loop PID controller has been studied to show a feasible accurate regulated performance for the difficult to control pneumatic muscle actuators (PMA). The artificial muscles used in this study were of rubber tubing with a braided nylon sheath, with muscle length of 75mm of which achieved strained 27mm contraction change in length. These PMA were used in the building of a dexterous manipulator of which utilises 18 of these new muscles to control 3 fingers and a thumb [28]. These muscles were observed to produce extremely high power-to-weight ratios averaging 1kW/kg, maximum contractile force of 50N with input tubing pressures of just 200kPa. Sufficiently, accurate control to 1 degree of finger joint rotational error, is attained using antagonistic paired PMA regulated by a closed-loop PID controller on experimental data instead of theoretical models. A high order and minimum order controller are designed of which both had a closed loop gain of 0.0425 [28]. Air pressure is provided using electrically driven, low-power piezoelectric valves with a switching frequency of 40-50Hz (Hoerberger piezo 2000, 0.001W per valve). This relatively rapid response made pulse width modulation under direct computer control feasible. And as such this was performed using a position sensor of which was sampled every 25ms and data used to update model and controller parameters [28]. The system is said to have focused on just computation and had not explored any memorisation models to optimise the process. This is a huge window of opportunity in which modern-day computational power can present a more robust control model.

2.2 Related Work

Related works to soft actuation weight reduction for increased power-to-weight ratio is explored by considering other means of soft muscle actuation in order to make an informed muscle design decision.

2.2.1 Alternative soft-robotic arm actuation using non-traditional pumps

In attempts to eliminate the undesired reliance on heavy externally situated pumps for fluidic soft muscles, Electrohydrodynamic stretchable pumps were used instead to be coupled with thinner walled fibre-like McKibben actuators, of which are referred to as Low Pressure Thin McKibben Muscles. These pumps act by accelerating liquid molecules using an electric field. Each muscle consists of a Stretchable pump – McKibben actuator pair of which cuts actuator weight drastically to 2g [29]. These pumps exhibit nonlinear force to contraction curve in producing a maximum contraction of 4mm (2.2% muscle length) in the McKibben fluidic muscle and ability to oppose a pulling force or weight at its end effector by 0.84N. This is attained by these pumps being able producing a resulting pressure of 0.24 kPa per microliter. Thus, it requires drastically lower fluidic volume of 83 microliters to produce 20kPa of pressure [29].

The interesting development of this study is the use of Thin McKibben Muscles (elastomer tubes of sizes of 1 mm sleeved in a fibre mesh) which improve in flexibility upon fluidic pressurisation as opposed to standard research dominating McKibben Muscles which stiffen on pressurisation and drastically decreases their extension with pressure. Bundled together in a sleeve, each Thin McKibben Muscles contributing 0.84N maximum force opposition on pressurisation by the Stretchable pumps can result in the total force being multiplied [29]. The use of Electrohydrodynamics as opposed to a mechanical pump to drive the pressurised flow however the Stretchable Pumps are limited by performance to drive high

pressure thus actuation of Thin McKibben Muscles by 100 to 200 kPa had to be reduced to 10-20kPa decreasing wall thickness of the elastomer to 0.15mm [29]. This increases the risk of failure in the muscle's integrity, overly increases its flexibility which may be undesirable to maintain the end of the actuator in a firm fixed position and its unsuitable use in resisting impact force with minimum deflection. Despite the high power to weight ratios of these pumps' fabrication of its laser-cut micrometre (400) electrodes and (23) polyethylene mask does not look easily plausible in attaining low-cost production. The research however shows coherence and statistically high reliability of such muscles in reproducing the exact same force with a maximum standard deviation of 0.0312N. Lastly a beneficial insight is the demonstration of the statistically approximate linear relation between pressure and force of McKibben muscles with negligible hysteresis. Forming the basis for their possible control.

2.2.2 Possibility for higher power agile soft actuators

A proposed an artificial muscle based on a thermal fabrication technique of inflatable actuators on sheet materials, in contrast to McKibben artificial muscle, has a free two-dimensional shape that is less than 0.1 mm thick. The research explores known morphologies of the muscles in anatomy, such as parallel/pennate muscles, and biceps/triceps muscles. These muscles equally have extremely high power to weight ratios with a produced sample of a 120 mm long and 50 mm wide rectangular muscle with a weight of 1.2g yielded a maximum output force of up to 35 N at a pressure of just 40 kPa [30]. Results conclusively asserted that the actuator can mimic the properties of the pennate muscle, which has angled muscle fibers. The sample was tested in a miniature jointed manipulator. The design also overcomes the form factor pitfall of the McKibben actuator limited to straight cylindrical bars. The research is well outlined in terms of fabrication of this novel technology, so it is reproducible. Using a CNC heat plotter (computer with soldering iron), sheets of thermoplastic

material, in this case, an aluminum-laminated polyethylene terephthalate (PET) film, were selectively welded to form gas-tight bladders, of which would later be air pressurized and act as the actuators. Results from this study also showed a larger tension force with a longer pouch however pouches longer than 20 mm tend to pop when subjected to a pressure of 40 kPa because of the increased area. Twice the pouch width doubles the tensile force [30].

Unfortunately, pressurization was done by an externally situated pump of which seldom had issues of the muscles being insufficiently supplied with air and falls well inline within the problem space of leveraging such potentially super powerful muscles without the unfavorable externally situated compressors and heavy equipment.

Chapter 3: Design & Methodology

This chapter details the design of the humanoid arm skeletal framework and muscle positioning and operability. The desired skeletal and muscle mapping, design requirements, technical specifications, are introduced in this chapter based on performance criteria and the humanoid arm use case. Preliminary dimensioning, and material selection are carried out based on secondary research and project objectives such as weight, cost and reliability.

3.1 Design Derivation and Constraints

The humanoid arm is conceptualized by studying the anatomical structure of the human arm. Each major joint, classified into shoulder (glenohumeral joint), elbow (elbow joint) and wrist (wrist joint) for the scope of this project, is modelled as a point mass with each limb member offering a degree of rotation about respective axes at the point masses.

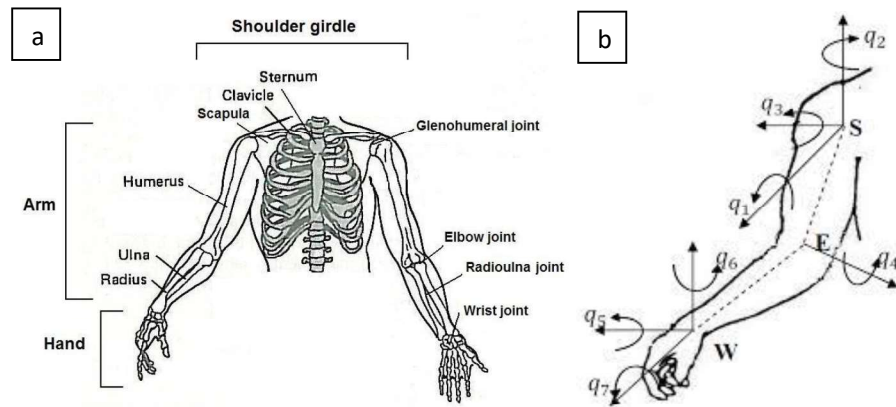


Figure 3.1: (a) Anatomy of arm [31], (b) Joint mapping for degrees of freedom [32]

Of proposed design, the human arm wholly comprises of 3 main sections: the hand, arm and shoulder girdle (Figure 3.1), of which the arm can then be subcategorized into the upper arm, forearm, wrist and hand. The upper arm encompasses the region of the arm between the shoulder and elbow joint and within the elbow girdle [31]. The kinematics of the scapula (shoulder blade) introduced a heightened level of complexity for the design of a humanoid arm

for robotic applications, as the bone mass of shoulder blade completely moves in its own action and does not present an expected hinged point mass translation for this humanoid arm design. Due to the complexity of the Ulna and Radius within the forearm realized by the turning of two parallel bones, the scope of the project presents a limitation in realizing a better achievable degree of freedom in supination/pronation of the forearm. The line of action of the arm and its skeletal link alters in motion, with the Radius bone actually twisting around the Ulna and changing its complete position in doing so. With the muscle McKibben Muscle choice to be used in the linear operation of the arm, such torsional action is additionally eliminated, excluding the proximal radioulnar joint at the elbow. Finally, for the wrist's flexion/extension achieved through the muscle contractions in the forearm, the wrist joint itself is realized by multiple architecture understudied in the design considerations for a similar iCub humanoid robot [33]. Comparing wrist joint architecture: the normal jointed, the gimbal, the spherical five-bar linkage, the spherical six-bar linkage, the OmniWrist-III and the Quaternion joint mechanisms offer 1-2 D.O.F and corresponding discontinuities/singularities and directional interdependencies [33]. The resulting wrist models and workspace analysis presented by the various 2 D.O.F joints are compared and shown to have efficient application in a cable-driven actuator system and have limited workspace range.

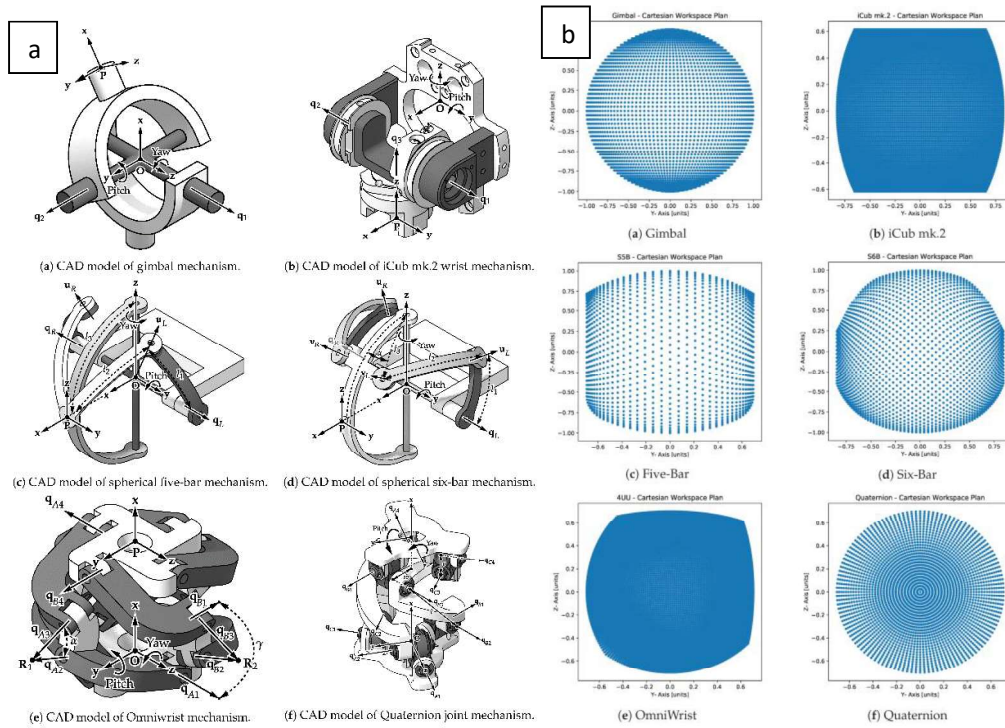


Figure 3.2: (a) Wrist joint architecture, (b) Normalized workspace angles [33]

The human wrist is normally able to achieve an abduction/adduction degree of freedom of approximately 50° . This compared to the joint modelling and comparisons made, presents just a narrow 27.7778% needed workspace rotation range about the y-axis. With additional joint singularities at the edges of the joints such as, a hinged joint for flexion/extension only, of close similarity to the iCub model would have to be designed as a proof of concept for this initial design of the humanoid arm, with room for being replaced with any of the aforementioned architecture.

The conclusive mapping of the musculoskeletal system for this project as such results in the following shortlisting:

Table 3.1: Joint determination and degrees of motion for humanoid arm

All Joints	Design Joints for project	Degree of Freedom
Shoulder (rotation)	Shoulder (rotation)	150°
Shoulder (abduction/adduction)	Shoulder (abduction/adduction)	90°
Shoulder (flexion/extension)	Shoulder (flexion/extension)	135°
Elbow (extension/flexion)	Elbow (extension/flexion)	115°
Elbow (pronation/supination)	-	-
Wrist (flexion/extension)	Wrist (flexion/extension)	66°
Wrist (abduction/adduction)	-	-

3.2 Humanoid arm performance evaluation criteria

The following evaluation criteria were generated as a result of the project goals and form the overarching benchmark for evaluating the design alternatives for the respective sections of the arm and the arm holistically.

Table 3.2: Evaluation criteria

Criteria	Description	Good Expected value	Best Expected Value
Cost	The arm must be of low cost without a considerable compromise on integrity and performance.	≤ \$4000	≤ \$2000
Weight	Arm must be lightweight, to achieve high-power to weight ratio specification.	≤ 5kg for arm only without power units (auxiliary components).	≤ 3kg for arm only without power units (auxiliary components).
Durability	Must have a high cycle use. Preferably to attain minimal component failure by fatigue.	Fatigue infinite life cycle (≥ 10 ⁶)	Fatigue infinite life cycle (≥ 10 ⁶)
Safety	Structural integrity of the arm must be high with a safe factor of safety under its loading scenarios, without overdesigning.	Overall F.O.S of 1 - 4	Overall F.O.S of 1.5 - 3
Biomimetic accuracy	Execute joint and limb motion to desired accuracy of the human arm	10% positional error	4% positional error

Sizing	Compact, small and modular, to be easily transported and assembled onto humanoid units, yet still meet the arm workspace range.	Reach 0.5m – 0.6m. Component sizing under 0.3m each and aligned to save space.	Reach 0.6m – 0.8m. Component sizing under 0.3m each and aligned to save space.
--------	---	---	---

3.3 Conceptual Designs and Selection

With an established joint and degree of freedom for the arm, the expected muscles to enable the actuation of such joints would be designed biomimetically to the human arm.

Conclusively, the humanoid arm can herein be broken down into 4 key modules. The limbs (limb material and sizing), the joints (joint material, type and sizing), the muscles (pneumatically actuated soft actuators) and the pneumatics and valve control mechanism (valve response, pressure rating, tubing and pump specification).

3.3.1 Skeletal framework/chassis preliminary designs

To closely model the humanoid arm and meet design specifications and functional requirements, the arm is foremostly oriented in the position as the human arm, with the shoulder joint plane oriented vertically in a presumed rest position. Its axis of rotation acts normal to the plane for the enabling of flexion and extension (lifting your arm upwards in front of you and moving the arm then backwards respectively). The orientation These form the only constraints in addition to the design specifications for arriving at concepts.

The following design concepts were arrived at:

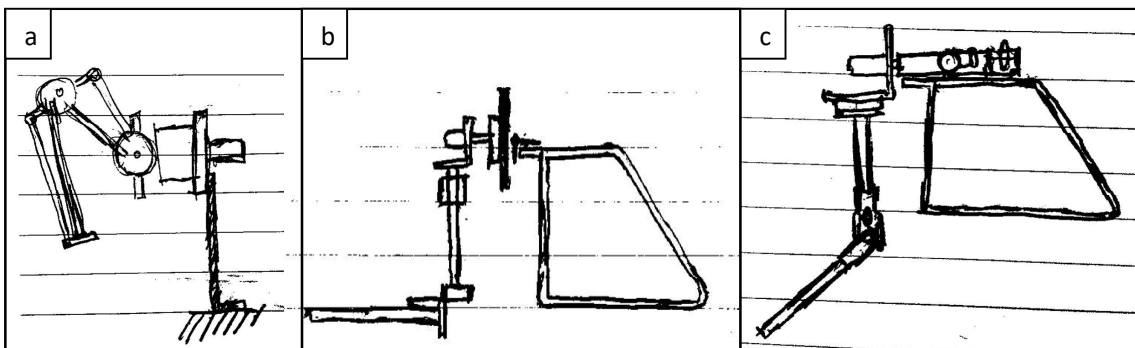


Figure 3.3: Conceptual design sketches (a) Design A, (b) Design B, (c) Design C

The designs are described in detail and each respective performance and likely issues outlined in the subsequent sub-sections.

3.3.2 Design A

The design primarily utilizes linkages with connecting rods at each circular joint. Each joint acts as a 3 joined pulley system, with the connecting rod running through one pulley, and the main limbs ending in attached free to rotate joints/pulleys. The connecting rods enable for a control rod/muscle to push forward or pull back on the rod, in turn rotating the pulley joint. Further design and sizing were modelled to meet the design specification, with limb lengths being 30cm each (forearm and upper arm).

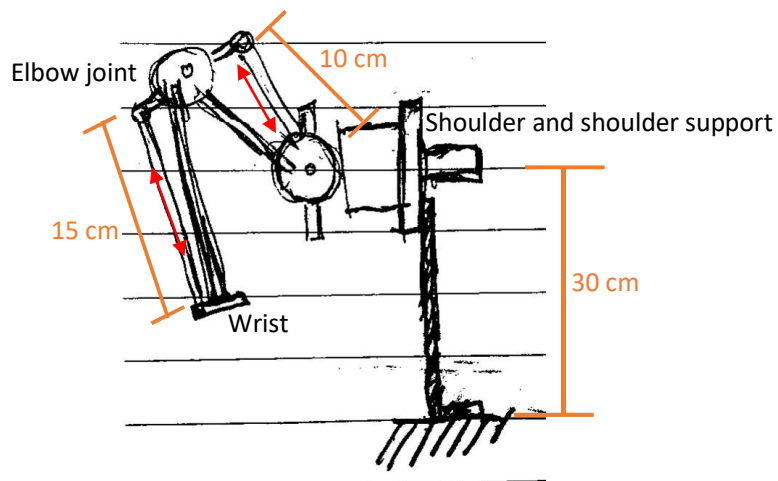


Figure 3.4: Overview of conceptual design A

The design makes it easier in creating large moments around the joints for higher load applications, as the connecting rod offers an increase perpendicular distance from the pulley pivot/axis.

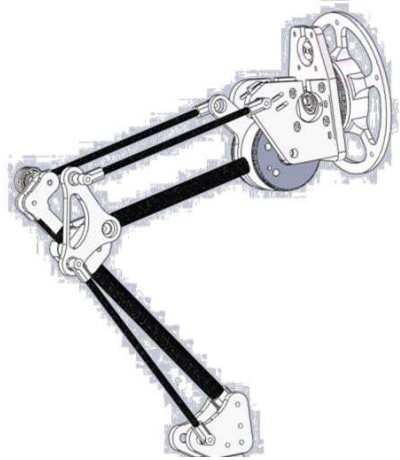


Figure 3.5: CAD model of conceptual design A

Upon CAD modelling the concept and undertaking a motion study, there were considerable limitations in the positioning of the arm and likewise the attachments of the muscles. There would be limited degrees of freedom from the expected 5 to 3. As each pulley joint presents a limitation in pronating or supinating in an axis perpendicular to its centre axis, i.e. the pulley/disc-like joints can only rotate about one axis. Additionally, there is considerable difficulty in fully straightening the arm. Conclusively the design lacks the biomimetic accuracy required.

3.3.3 Design B

The design utilizes simple hinges in the elbow, wrist and shoulder. The shoulder plate component acts as a shoulder socket to which the L-shaped shoulder joint attaches to. By a thin rod. This allows for the entire shoulder socket to be hinged about one axis to the support frame (chest), and the L-shape shoulder to utilize the remaining degrees of freedom to its two faces: flexion/extension through the face linked to the hinged shoulder socket, and rotation to the forearm rod connected on its lower face. To minimize rotational friction the rods are intended to be fixed withing bearings at the aforementioned locations only. Thus the 5 D.O.F specification can be met: 3 D.O.F shoulder, 1 D.O.F elbow, 1 D.O.F wrist.

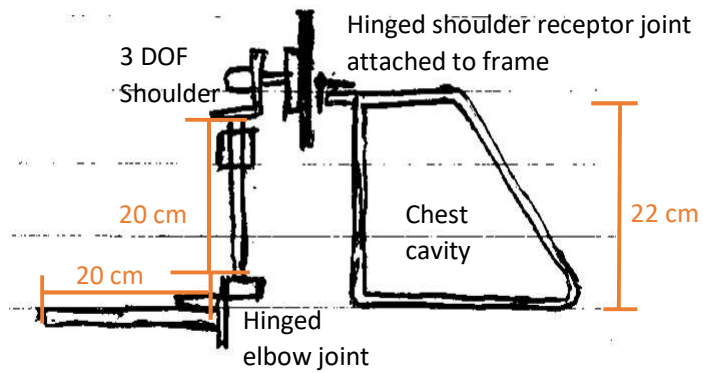


Figure 3.6: Overview of conceptual design B

The support frame is modelled from a 6cm wide, 2.5mm thick plate and is intended to be clamped down on its base for mounting. The free space within this support is intended to house the arm's miniature pump, and pressure tubing and valve system. With a void dimension of approximately, this closely matches to the internal room of the humanoid body of which houses similar components and auxiliary units. Analysis of the preliminary CAD model of the arm demonstrates an accurate biomimetic motion and required workspace manoeuvrability and reach.



Figure 3.7: CAD model of conceptual design B

However, despite having met the biomimetic accuracy, the intended muscle design and locations would:

- Cause excessive muscle strain
- Muscle twisting around limb
- Inconsistent muscle positioning and thus varied discontinued acting forces and calculations
- Unequal muscle sizing of antagonistic pairs, thus unequal pressure control and muscle characteristics.

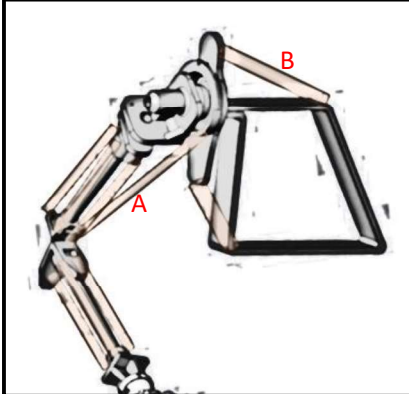
	Symbol	Complication
	A	Twisting of the shoulder flexion/abduction muscle around upper arm during upper arm rotation
	B	Unequal sized antagonistic muscle pair for shoulder abduction/adduction (elevation)
	A	Siting of the shoulder flexion/extension muscles in the upper arm from the elbow to the shoulder is ineffective in driving high torque

Figure 3.8: Arm mobility and muscle limitations in design B

3.3.4 Design C

Of close similarity to Design B, C leverages the biomimetic accuracy of the human arm design replicated in B and maintains the same structural orientation and support.

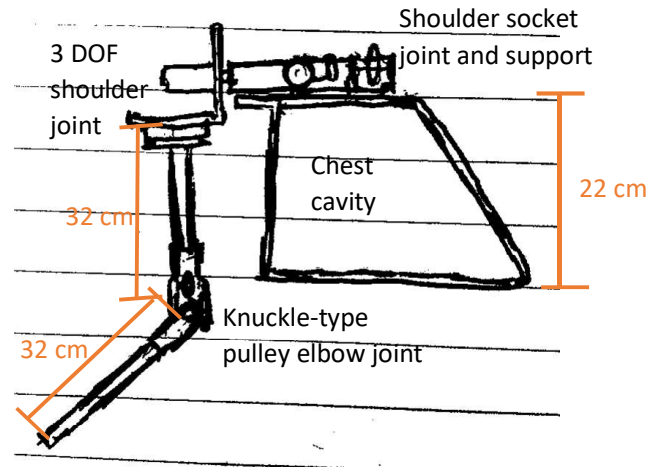


Figure 3.9: Overview of conceptual design C

However, this design seeks to improve the muscle design location and improve the joint design to enable smoother and rotations. The elbow joint is replaced with a knuckle-type joint of coupled pulley to keep the muscle link to the skeletal structure aligned during action and taut. The design eliminates the need to mount the shoulder flexion/extension muscle within the arm and rather utilizes a designed double cardan extensor joint (component highlighted in orange in CAD model, Figure 3.10) within the shoulder socket. This allows for the shoulder muscles to be biomimetically mounted within the chest void and accurately control the shoulder without twisting or a change in its orientation. All muscles pairs can thus be of correct sizing to each other and demonstrate equal and opposite extension and pressurization in each antagonistic pair. Additionally, lightweight small bearings are included in the design to defined contact points for the muscles, as such the known muscle lengths can be determined based on the original length of the linkages in neutral orientation and the final distance (and extended length, i.e Final distance – Initial orientation distance) between muscle contact points. Hooking the muscles to these points also provide stability to keep the muscle force acting continuous in the correct direction and also helps elevate the muscles from the skeletal structure, so during muscle contraction there is room for lateral expansion of the muscle.

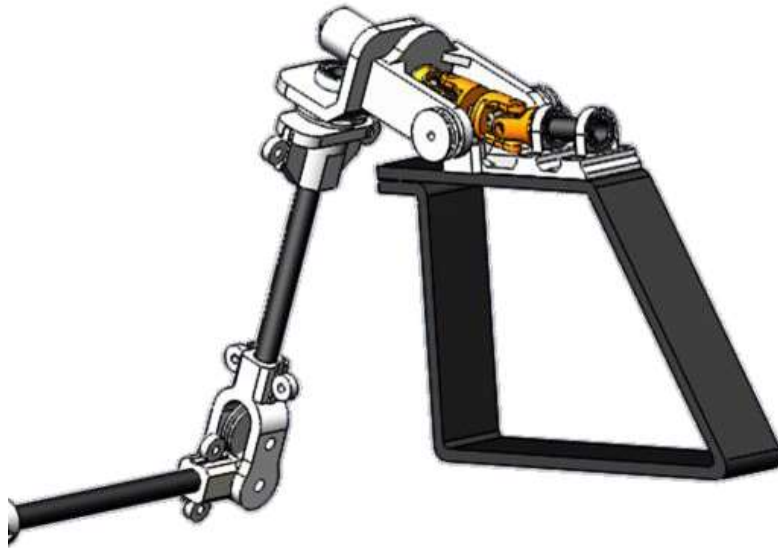


Figure 3.10: CAD model of conceptual design C

In accordance with the functional requirements, for speed of production, lower cost and weight specification, components such as the joint are modelled to decrease complexity without compromising strength, but additionally be reproducible and hackable by choosing 3D printable high-strength low-weight joint designs.

3.3.5 Skeletal framework selected design

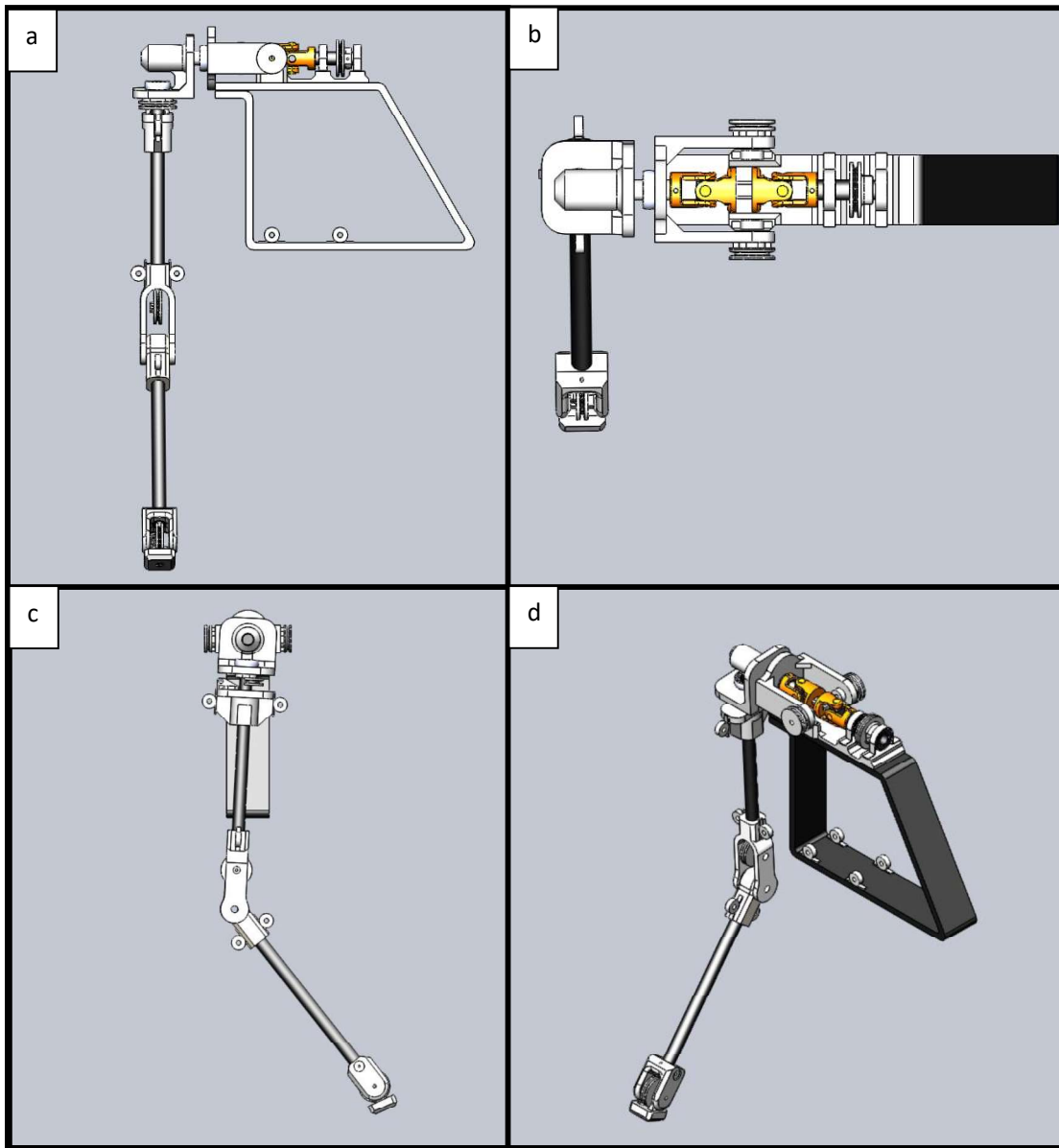


Figure 3.11: CAD model perspectives of final design; (a) Front view, (b) Top view, (c) Left view, (d) Isometric view

Based on the aforementioned design limitations and improvements, the selected design is Design C, of which would further accurately be designed and mechanically assessed. Details of the design are included in the appendix, after thorough sizing and material selection in this chapter.

3.4 Key Component Selection

The key components are material, type and design specified in this sub-section. Of configuration/material selection a product matching the respective selections are detailed where appropriate.

3.4.1 Valve system configuration

In addition to the existing evaluation criteria for the humanoid arm's overall performance, the biomimetic accuracy in terms of control is further elaborated and broken down into the muscle valve control's response time, and circuitry integration.

Table 3.3: Pugh chart for valve system selection

Criteria	Weight (0.0-1.0)	3/2-way monostable Solenoid (Score: 0-5)	3/2-way bistable Solenoid (Score: 0-5)	5/3-way Pressure Holding Center Solenoid (Score: 0-5)
Cost	0.3	3	3	4
Weight	0.1	3.5	3.5	4
Durability	0.05	4	4	5
Safety	0.1	5	5	5
Biomimetic accuracy	0.05	3	4	5
Response time	0.25	5	5	5
Sizing	0.05	5	4.75	3
Integration	0.1	5	5	5
TOTAL (Summed weighted score)	1	4.1	4.1375	4.5

To raise the sizing score and weight scores of the 5/3-way PHC solenoid valves, the valve specified for this project is Sub-miniature pilot 5/3-way solenoid valve with a Wattmizer Proportional Two Way Normally Closed Valves. These are extremely light weight, small and high pressure tolerant as detail in their specification sheet in Appendix D and E.

3.4.2 Soft actuator system configuration

Of major importance for the actuation of the humanoid arm is the choice of pneumatic Artificial Muscle type to be utilized for the proof of concept. The configuration listing is arrived at through secondary research and literature research along the project goals. The intended purpose of the project is to untether the soft actuator from an external pressure unit; thus, the chosen muscle types must be able to work under the power of an embedded pump, be applicable with millimetre tube sizing and ease of attachment to the skeletal contact points in the design (Integration).

Table 3.4: Pugh chart for soft actuator system selection

Criteria	Weight (0.0-1.0)	HASEL Muscle (Score: 0-5)	McKibben Tubing (Score: 0-5)	Linear PAM (Score: 0-5)
Cost	0.3	2	5	3
Weight	0.1	3.5	3.5	4
Durability	0.1	4	4	5
Safety	0.1	5	5	5
Biomimetic accuracy	0.2	3.5	4.5	4
Integration	0.1	5	4	4
Sizing	0.1	5	4.75	3
TOTAL (Summed weighted score)	1	3.55	4.525	3.8

Conclusively, the arm would use McKibben Tubing as its soft actuators. McKibben muscles are elastic tubing encased within an expansible nylon mesh sheath. Upon pressurizing, the tubing expands, and the sheath equally opens up laterally, however with the braid pattern, causes a shortening in length of the sheath, effecting a muscle contraction and vice versa for depressurization.

3.4.3 Limb primary material selection

From the design selection made, the limb rods are hollowed cylindrical rods whose material choice primarily would have prioritization for strength and stiffness. However, considering the project goal and application area, cost is an equal dominant factor as well as

the material density. Using the CES EduPack Material Selection software, the following materials were chosen for consideration haven met a considerable performance region for our intended application. The sizing and thickness of the rods/tubes are determined by stress analysis in the preceding subsections.

Table 3.5: Pugh chart for limb material selection

Criteria	Weight (0.0-1.0)	Mild Steel AISI 1020 (Score: 0-5)	Aluminum (Score: 0-5)	Thermosetting Polymers (Score: 0-5)
Cost	0.2	4	4.5	4
Weight	0.1	3	5	5
Durability	0.1	4.5	3	2
Safety	0.3	5	3.5	2
Biomimetic accuracy	0.1	5	4.75	3
Sizing	0.2	4.5	4	5
TOTAL (Summed weighted score)	1	4.35	4.025	3.4

Selected material is Mild Steel AISI 1020 for the hollow round rod:

- $S_{ut} = 470\text{MPa}$
- $S_{yt} = 395\text{MPa}$

3.4.4 Limb joint material selection

The material to be chosen for the lightweight high-strength joints is to be 3D-printable.

Table 3.6: Pugh chart for limb joint material selection

Criteria	Weight (0.0-1.0)	3/2-way monostable Solenoid (PLA) (Score: 0-5)	3/2-way bistable Solenoid (ABS) (Score: 0-5)
Cost	0.3	4	3
Weight	0.25	3.5	3.5
Durability	0.2	3	5
Safety	0.2	5	5
Sizing	0.05	5	4.75
TOTAL (Summed weighted score)	1	3.925	4.0125

Selected material is ABS:

- $S_{ut} = 80\text{MPa}$
- $S_{yt} = 28\text{MPa}$

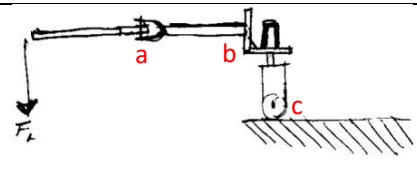
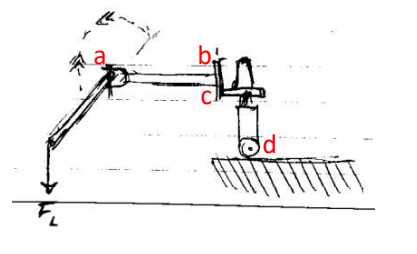
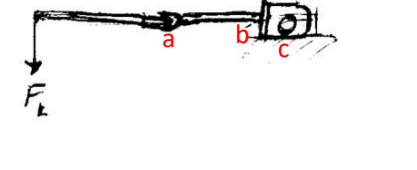
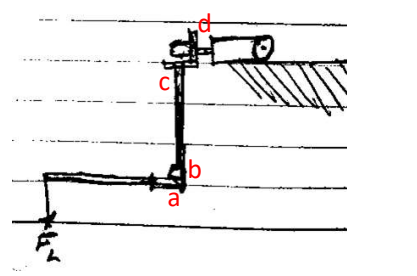
3.5 Modelling the Arm's Mechanical Operation

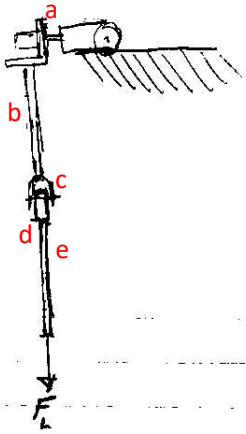
3.5.1 Operational loading scenarios

To determine the mechanical stresses and possible failure points, the arm is modelled at various orientations that either result in the maximum bending stress, maximum torsional stress and maximum tensile stress while supporting a weight at its end. Thus, for instance, in abduction of the arm, a full 90 lift induces the largest bending stress at the shoulder and largest torsional stress at the shoulder joint as the moment created at this angle is the largest due to the largest perpendicular distance of the line of action of the load to the pivot point. This modelling is repeated for different scenarios and the maximum effects at each joint identified and analysed at critical positions with the expected load force F applied at the end. The different loading cases are then identified (Case ID) and scenarios in which an existing loading case either causes a bending, tension or torsional load than the one identified are not included. The larger loading effect on the same joint of same load type is giving precedence and rather calculated for. For instance, a bending stress at the shoulder by loading the arm's end in full extension is much larger than the arm in half extension (i.e., forearm flexed, perpendicular distance of load action from shoulder pivot is halved) thus the latter is ignored and the first calculated for at the shoulder for bending. These result in calculations for the maximum stress scenarios at the critical joint induced by the load and the arm's orientation. This methodology does not seek to ignore the existence of multiple stresses in the arm during operation, but model and try arriving at the worst-case scenario of loading to calculate the minimum sizing and factor of safety values

before performing a more holistic stress analysis to encompass all other evident stresses and stress points in the preceding chapter.

Table 3.7: Arm extreme orientations and loading effects

Arm orientation	Perspective	Description	Loading – Critical Location – Location in arm orientation diagram (Case ID)
	Front view	Shoulder lifted up near 90° (abduction) and forearm in full extension.	Bending – Elbow – a (Case 1A) Bending – Shoulder – b (Case 1B) Torsion – Shoulder – c (Case 1C)
	Front view	Shoulder lifted up near 90° (abduction) and forearm in flexed to near 90°.	Bending – Elbow – a (Case 2A) Torsion – UpperArm - b (Case 2B) Bending – Shoulder – c (Case 2C) Torsion – Shoulder – d (Case 2D)
	Left view	Shoulder level, arm tilted back/forward near horizontal. Forearm in full extension.	Bending – Elbow – a (Case 3A) Bending – Shoulder – b (Case 3B) Torsion – Shoulder – c (Case 3C)
	Front view	Shoulder level/unelevated. Upper arm rotated outward by near 90° left from center rest position, rotation has no effect on load scenario, as upper arm remains vertically below shoulder. Forearm flexed to near 90°.	Bending – Elbow – a (Case 4A) Tension – Elbow – b (Case 4B) Tension – UpperArm – c (Case 4C) Bending – Shoulder – d (Case 4D)

	Front view	Shoulder level and not elevated. Arm in full flexion vertically down.	Bending – Shoulder – a (Case 5A) Tension – Upper Arm – b (Case 5C) Tension – Elbow Upper – c (Case 5D) Tension – Elbow Lower – d (Case 5E) Tension – Forearm – e (Case 5F)
---	------------	---	--

3.5.2 Identifying loading cases for highest stresses at joints/limbs

To identify the largest loading cases, a comparison table is created to compare the theoretical stress to be resulted in each joint and arrive at the load conditions that create these highest stress conditions and are not surpassed by any other load case.

Table 3.8: Arm load case comparison for maximum loading effects

Loading case	Load effect similar to other Case:	Load effect surpassed by other Case:
Case 1A	Case 3A	—
Case 1B	Case 3B	—
Case 1C	—	—
Case 2A	Case 4A	Case 1A
Case 2B	—	—
Case 2C	—	Case 1B
Case 2D	—	Case 1C
Case 3A	Case 1A	—
Case 3B	Case 1B	—
Case 3C	—	—
Case 4A	Case 2A	Case 1A
Case 4B	Case 5D	—
Case 4C	Case 5C, Case 5F	—
Case 4D	Case 5A	—
Case 5A	Case 4D	—
Case 5C	Case 4C, Case 5F	—
Case 5D	Case 4B	—
Case 5E	—	—
Case 5F	Case 5C	—

Thus, the load cases 1A, 1B, 1C, 2B, 3A, 3B, 3C, 4B, 4C, 4D, 5A, 5C, 5D, 5E and 5F, are not surpassed by any other loading scenario due to the arm's orientation. For Case 5F as the limbs are to be made of the same diameter, rod thickness and of the same 27cm length, the stresses within the limbs are similar for the same applied load. However, of these selected cases, some cases are of similarity in the loading effect at the respective joints. The case 1C, results in the identified torsion transmitted to a bolt holding the joint in place and then to the muscles, thus a torque of $\approx 54\text{Nm}$ using a torque calculator does not approach the failure limit for a 3.5mm high steel bolt to be used in design, assisted by the muscle's supportive force. Thus, the final selection of cases to design for are: 1A, 1B, 2B, 3C, 4B, 4D and 5E. These calculations are used to analytically determine preliminary thresholds for the dimensions of the limbs and joints, and factor of safety. These preliminary sizing are used in the final CAD modelling of the humanoid arm, and then a better detailed Finite Element Analysis is performed on all arm components designed and sized.

3.6 McKibben Muscle Design and Sizing

This subsection determines the muscle extension and force generation required to operate the arm. This is done so by computing the total distance the muscle is required to extend/contract by having been antagonistically paired, using the required angular displacement of the joint, θ , and the pulley radius, r , it is tethered to:

$$S = \theta r \quad (\text{Eq. 1})$$

For each joint, the maximum torque is determined from the different load cases, for which the arm must drive its own section weight and payload of 88.29 N (Appendix B). Then the holding force, F_H , a muscle must ascertain to support this torque is determined using the joint's pulley radius, r :

$$F_H = T/r \quad (\text{Eq. 2})$$

With known approximate response of 0.1s. Then the approximate acceleration of the muscles during full extension from a contraction and vice. versa contraction, is:

$$a = S/0.1 \quad (\text{Eq. 3})$$

Then as such, the acceleration force is given by multiplying the mass, m , (payload and arm section weight) for each joint motion (Appendix B) by the obtained acceleration:

$$F_A = 10 \times S \times m \quad (\text{Eq. 4})$$

The total maximum generative force of the muscles must then be a summation of the force to accelerate the muscle during operation and then hold the maximum payload at the arrived positions.

3.6.1 Muscle loading and extensions for wrist flexion/extension

For the wrist joint, the pulley (indicated in orange below) is required to attain an angular displacement of up to 66° (1.15192 rad), thus calculating for the maximum extension to drive the connecting cable at the pulley circumference:

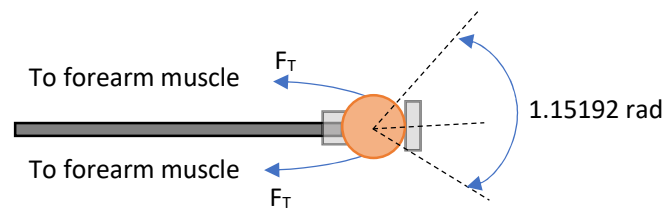


Figure 3.12: Forearm muscles FBD analysis for wrist joint flexion/extension

Table 3.9: Calculated wrist joint muscle flexion/extension properties

Property	Value
Joint D.O.F, θ / rad	1.15192
Pulley radius, r / mm	17
Maximum muscle extension/contraction, S / mm	19.583
Single muscle contraction/extension from rest / mm	± 9.791
Holding force, F_H / N	88.29
Accelerating force, F_A / N	1.77505

3.6.2 Muscle loading and extensions for elbow flexion/extension

For the elbow joint, the circumferential region (indicated in orange below) is required to attain an angular displacement of up to 115° (2.00713 rad), thus calculating for the maximum extension to drive the connecting cable at the pulley circumference:

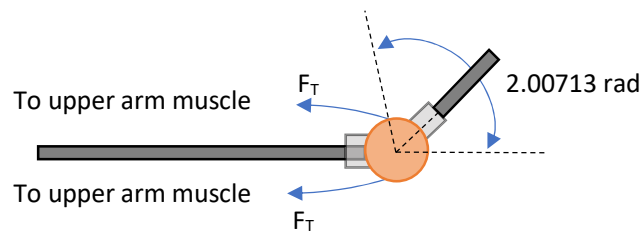


Figure 3.13: Upper arm muscles FBD analysis for elbow joint flexion/extension

Table 3.10: Calculated elbow joint muscle flexion/extension properties

Property	Value
Joint D.O.F, θ / rad	2.00713
Pulley radius, r / mm	17
Maximum muscle extension/contraction, S / mm	34.121
Single muscle contraction/extension from rest / mm	± 17.061
Holding force, F_H / N	1518.34
Accelerating force, F_A / N	3.11583

3.6.3 Muscle loading and extensions for shoulder rotation

For the shoulder's rotational joint, the pulley positioned at the contact point of the upper arm (indicated in orange below) is required to attain an angular displacement of up to 150° (2.61799 rad), thus calculating for the maximum extension to drive the connecting cable at the pulley circumference:

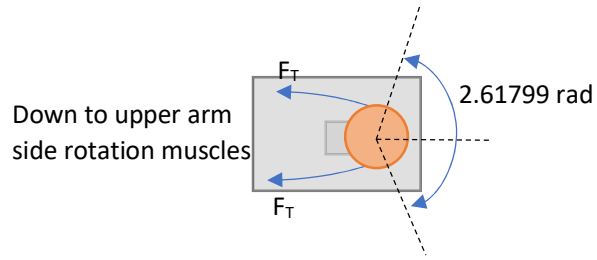


Figure 3.14: Upper arm muscles FBD analysis for upper arm shoulder rotation

Table 3.11: Calculated shoulder joint muscle rotational drive properties

Property	Value
Joint D.O.F, θ / rad	2.61799
Pulley radius, r / mm	20
Maximum muscle extension/contraction, S / mm	52.3598
Single muscle contraction/extension from rest / mm	± 26.1799
Holding force, F_H / N	1350.75
Accelerating force, F_A / N	4.78135

3.6.4 Muscle loading and extensions for shoulder flexion/extension

For the shoulder's flexion/extension joint, the pulley is positioned on the chest support behind the double cardan joint, with the shoulder rod passing through. This joint is required to attain an angular displacement of up to 135° (2.35619 rad), thus calculating for the maximum extension to drive the connecting cable at the pulley circumference:

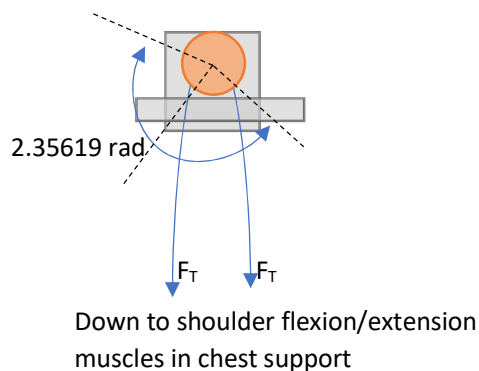


Figure 3.15: Shoulder muscles FBD analysis for shoulder joint flexion/extension

Table 3.12: Calculated shoulder joint muscle flexion/extension properties

Property	Value
Joint D.O.F, θ / rad	2.35619
Pulley radius, r / mm	18.75
Maximum muscle extension/contraction, S / mm	44.179
Single muscle contraction/extension from rest / mm	± 22.089
Holding force, F_H / N	1577.51
Accelerating force, F_A / N	4.06383

3.6.5 Muscle loading and extensions for shoulder abduction/adduction

For the shoulder's elevation joint, the pulley (indicated in orange below) is positioned as the end of the shoulder socket that connects the chest plate component. This joint is required to attain an angular displacement of up to 90° (1.5708 rad), thus calculating for the maximum extension to drive the connecting cable at the pulley circumference:

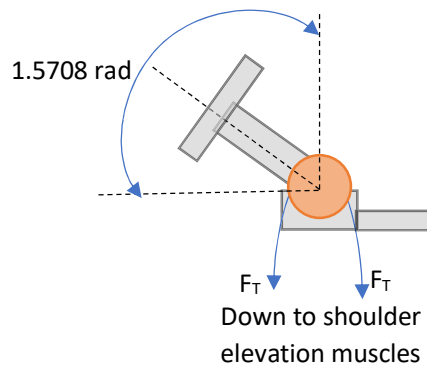


Figure 3.16: Shoulder muscles FBD analysis for shoulder joint abduction/adduction

Table 3.13: Calculated shoulder joint muscle abduction/adduction properties

Property	Value
Joint D.O.F, θ / rad	1.5708
Pulley radius, r / mm	15
Maximum muscle extension/contraction, S / mm	23.562
Single muscle contraction/extension from rest / mm	± 11.781
Holding force, F_H / N	1732.32
Accelerating force, F_A / N	2.16736

3.7.6 Summary of Muscle load operations

McKibben tubing comprises of a latex/silicone inner tubing of which when pneumatically pressurizes swells and expands in the lateral direction normal to its thin walls. However, encasing these tubes in a braided nylon sleeving/sheath, results in a controlled directional expansion. The sleeve braid pattern is pushed back at a greater angle as the sleeve also expands laterally, however of fixed sleeve length, this causes the sleeve to contract and shorten to maintain the initial volume definition.

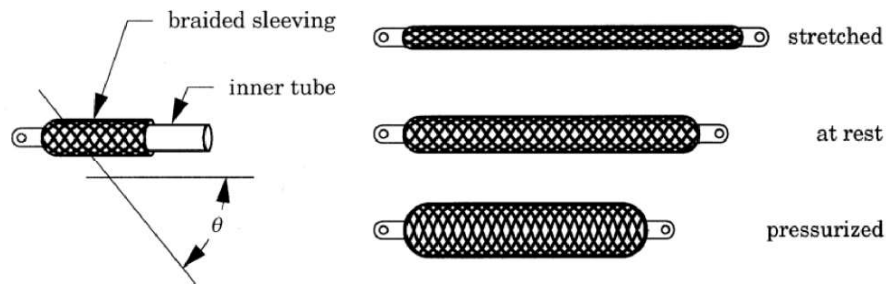


Figure 3.17: McKibben tubing overview [34]

The load and extension calculations obtained for each antagonistic muscle pair is summarized in the table below. Where each half of an antagonistic pair comprises of two of the same muscles in order to share and reduce the total driving force per muscle to a manageable range for operation without the need of extremely high pressure per muscle. I.e. For each antagonistic pair there are a total of 4 muscles, 2 per opposing direction.

Table 3.14: Summary of paired muscles' maximum force and contractions

Antagonistic pair	Total force required / N	Maximum force per muscle / N	Maximum muscle contraction / m
Forearm muscles flexion/extension at wrist	90.065	45.0325	0.009791
Upper arm muscles for flexion/extension at elbow	1521.46	760.73	0.017061
Upper arm muscles for rotation of upper arm at shoulder	1355.53	677.765	0.0261799
Shoulder flexion/extension muscles in chest	1581.57	790.5	0.022089

Shoulder abduction/adduction muscles in chest, for shoulder elevation	1734.49	867.245	0.011781
---	---------	---------	----------

3.7 Determining required muscle performance

Utilizing a sigmoid function from experimental extension modelling proposed by Alaa Al-Ibadi, the muscle extension can be related to the required pressure and initial muscle length. This researched sigmoidal function [35] adopted from Tondu and Lopez [36] has been expressed in terms of contraction, e , and not extension. To deduce the pressure constraint, the model of the extension force is introduced and negated due to the inward direction of the output force during contraction.

$$F = \pi r_0^2 P \left[\frac{3}{\tan^2 \theta_0} \left(1 - \frac{e}{L_0} \right) - \frac{1}{\sin^2 \theta_0} \right] \quad (\text{Eq. 5})$$

Where F = the muscle's produced force

θ_0 = the initial braid angle to the cylindrical axis of the braided sleeve

r_0 = the initial radius of the muscle

This project would seek to validate this novel model introduced, but for muscle contraction as opposed to extension and test its overall performance as a linear actuator in the humanoid arm. The governing assumptions proposed by Tondu and Lopez [36] implied the criteria for selecting a thin, almost negligible, walled latex tube for this muscle application.

Based on the modelled design and muscle bill of materials, the muscle initial length, L_0 of 17cm were used, of which accommodates for the calculated muscle extensions without being impeded by contact with the skeletal structure. Of equal lengths connected taut to their pulleys, the range of muscle can be deduced to be a function of the provided radius and pressure. The larger the radius, the larger the extension/contraction to maintain the muscles sleeve volume.

Table 3.15: Muscle dimensions

Antagonistic pair	Initial radius / m	Initial length / m
Forearm muscles flexion/extension at wrist	0.003175	0.18
Upper arm muscles for flexion/extension at elbow	0.009525	0.18
Upper arm muscles for rotation of upper arm at shoulder	0.009525	0.18
Shoulder flexion/extension muscles in chest	0.009525	0.18
Shoulder abduction/adduction muscles in chest, for shoulder elevation	0.009525	0.18

Having determined the muscle constants, the maximum pressures can be calculated for and the respective no-load extension range the muscles can attain. The rest length of braided sleeve has a measured braid angle, θ_0 of approximately 0.436332 rad (25°).

Using L_0 , F , maximum contraction as e , and r_0 values from Table 3.14 and Table 3.15, Eq. 5 is used to estimated maximum pressure required can be determined for the muscles.

Table 3.16: Muscles maximum operational pressures

Antagonistic pair	Maximum Pressure at F_T / Pa
Forearm muscles flexion/extension at wrist	190935
Upper arm muscles for flexion/extension at elbow	387367
Upper arm muscles for rotation of upper arm at shoulder	384084
Shoulder flexion/extension muscles in chest	426375
Shoulder abduction/adduction muscles in chest, for shoulder elevation	417106

Thus, the muscle system has a required pressure rating of 4.26375 Bar (426.375 kPa). The project utilizes the AIRPO D2028B Miniature-pressure pumps for the purpose of muscle performance testing in this (Datasheet attached in Appendix F). The 12V DC Voltage rating makes them ideal for onboard circuitry without the need for external high voltage power tethering. Their lightweight miniature size makes them suitable for the embedded pump system design goal.

Chapter 4: Analysis

This chapter explores the detailed load analysis (analytically and numerically) and stress effects on the skeletal structure of the humanoid arm. The required muscles are also fabricated and experimentally analysed for performance and cyclic accuracy before its incorporation into the humanoid arm.

4.1 Analytical Analysis

This subsection delves into the stress analysis of the skeletal structure, with the chosen mechanical parts and materials, to determine an estimated factor of safety and component dimensions. The stress calculations performed in the respective tables have each respective variable calculated using the formulas below of which primarily start with the exerted load, applied moment/torsion and the material and its sizing.

The fatigue analysis utilizes the equations for calculating the von Mises Normal Stresses as [37]:

$$\sigma'_m = (\sigma_m^2 + 3\tau_m^2)^{\frac{1}{2}} \quad (\text{Eq. 6})$$

$$\sigma'_a = (\sigma_a^2 + 3\tau_a^2)^{\frac{1}{2}} \quad (\text{Eq. 7})$$

Design calculations are performed by considering the Modified Goodman criterion for fatigue analysis of which has governing equations [37]:

For material mean and alternating strengths, S_m and S_a respectively:

$$S_m = \frac{(S_y - S_e)S_{ut}}{S_{ut} - S_e} \quad (\text{Eq. 8})$$

$$S_a = S_y - S_m \quad (\text{Eq. 9})$$

Of determined likely failure by fatigue from having a lower fatigue factor of safety than yielding, this factor of safety, n, can be determined by:

$$\frac{1}{n} = \frac{\sigma_m}{S_{ut}} + \frac{\sigma_a}{S_e} \quad (\text{Eq. 10})$$

Using MEDT failure criterion for static analysis of which has governing equations:

$$\sigma_e = (\sigma_1^2 - \sigma_1 \sigma_2 + \sigma_2^2)^{\frac{1}{2}} \quad (\text{Eq. 11})$$

$$\frac{1}{n} = \frac{\sigma_m}{S_{ut}} + \frac{\sigma_a}{S_e} \quad (\text{Eq. 12})$$

4.1.1 Analysis of Load Case 1A

In this arm orientation, there is a resultant Bending at the elbow joint.

Sketch of Case 1A, is the forearm, connection of forearm to elbow and elbow:

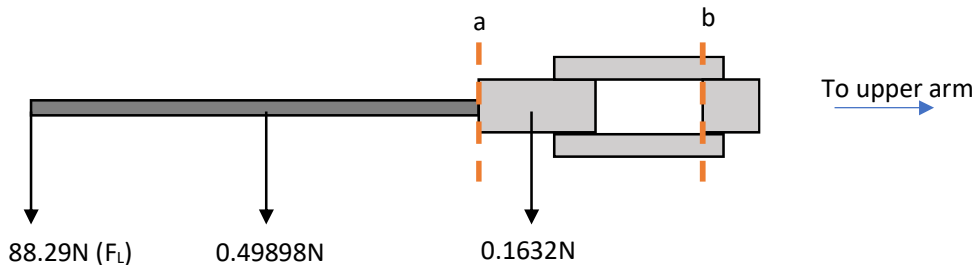


Figure 4.1: FBD and load analysis of forearm-elbow section in load case 1A

Identified critical locations: limb joint (a) for failure in the limb, and thin joints of plastic elbow (b) for failure in the plastic. Assuming fixed at b.

Table 4.1: Static/Yield analysis of forearm-elbow section in load case 1A

Critical location	a	b
Bending moment / Nmm	23905.7	30573
Cross-section	 Inner d = 15mm Outer d = 17.5mm	 h = 40mm b = 10mm

Bending stress / MPa		98.7228	5.73244 (for one side) *
Principal stresses	σ_1 /MPa	98.7228	5.73244
	σ_2 /MPa	0	0
	σ_3 /MPa	0	0
Material properties		Mild steel AISI 1020 Cold drawn Ductile $S_y = 395$ MPa	ABS Ductile polymer $S_y \approx 28$ MPa
Design Equation		MDET	MDET
Calculated Factor of Safety		4.0011	4.88448

Table 4.2: Fatigue analysis of forearm-elbow section in load case 1A

Critical location		a	b
Cyclic loading type		Fully reversed	Fully reversed
Bending moment / Nmm		23905.7	30573
Cross-section		 Inner d = 15mm Outer d = 17.5mm	 h = 40mm b = 10mm
Bending stress, σ_x / MPa		98.7228	5.73244 (for one side) *
Mean: σ_m / MPa		0	0
Alternating: σ_a / MPa		98.7228	5.73244
Von Misses	σ_m' / MPa	0	0
	σ_a' / MPa	98.7228	5.73244
Material properties		Mild steel AISI 1020 Ductile $S_y = 395$ MPa $S_{UT} = 470$ MPa	ABS Ductile polymer $S_y \approx 28$ MPa
Specimen Endurance Limit, S_e' / MPa		235	—
Marin Correction Factors	k_a	1.09342 (Cold drawn)	—
	k_b	0.912886 (Bending, round, rotating**)	—
	k_c	1 (bending)	—
	k_d	1 (Operation at r.t.p)	—
	k_e	1 (50% reliability min)	—
	k_f	1 (No miscellaneous effects)	—
Endurance strength, S_e / MPa		234.569	—
Failure Criterion		Modified Goodman	—
S_m		320.275	—
S_a		74.7254	—
Slope of reference line, $r_c = S_a/S_m$		4.28603	—
Slope of load line, $r_L = \sigma_a/\sigma_m$		Along σ_a since $\sigma_m = 0$	—
Determined means of failure if failure is to occur		Fatigue	—
Calculated Factor of Safety		2.37604	—

* The joint at section a comprises of two cross-sections supporting the bending stress equally.

** Designing for the worst use case where arm is rotating/turning while being loaded/unloaded.

Due to the unavailability of public research information on the S-N curve for ABS material, the endurance limits of the material cannot be easily determined, as such would be calculated through Finite Element Analysis by means of SolidWorks to determine the existing strength and design factor of safety more accurately.

4.1.2 Analysis of Load Case 1B

In this arm orientation, there is a resultant Bending at the shoulder joint.

Sketch of Case 1B, is the forearm, elbow, and upper arm leading to shoulder joint:

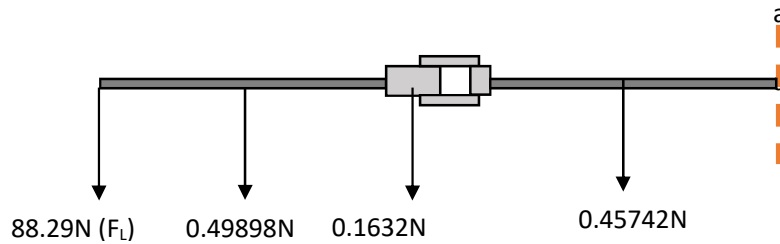


Figure 4.2: FBD and load analysis of full arm length in load case 1B

Identified critical location: limb joint (a) for failure in the limb. Assuming fixed at a.

Table 4.3: Static/Yield analysis of upper limb fixed point in load case 1B

Critical location		a
Bending moment / Nmm		51969.5
Cross-section		 Inner d = 15mm Outer d = 17.5mm
Bending stress / MPa		214.617
Principal stresses	σ_1 / MPa	214.617
	σ_2 / MPa	0
	σ_3 / MPa	0

Material properties	Mild steel AISI 1020 Ductile $S_y = 395 \text{ MPa}$
Design Equation	MDET
Calculated Factor of Safety	1.84049

Table 4.4: Fatigue analysis of upper limb fixed point in load case 1B

Critical location	a	
Cyclic loading type	Fully reversed	
Bending moment / Nmm	54680	
Cross-section	 Inner d = 15mm Outer d = 17.5mm	
Bending stress, σ_x / MPa	214.617	
Mean: σ_m / MPa	0	
Alternating: σ_a / MPa	214.617	
Von Misses	σ_m^* / MPa	0
Normal Stresses	σ_a^* / MPa	214.617
Material properties	Mild steel AISI 1020 Ductile $S_y = 395 \text{ MPa}$ $S_{UT} = 470 \text{ MPa}$	
Specimen Endurance Limit, S_e^* / MPa	235	
Marin Correction Factors	k_a	1.09342 (Cold drawn)
	k_b	0.912886 (Bending, round, rotating*)
	k_c	1 (bending)
	k_d	1 (Operation at r.t.p)
	k_e	1 (50% reliability min)
	k_f	1 (No miscellaneous effects)
Endurance strength, S_e / MPa	234.569	
Failure Criterion	Modified Goodman	
S_m	320.275	
S_a	74.7254	
Slope of reference line, $r_c = S_a/S_m$	4.28603	
Slope of load line, $r_L = \sigma_a/\sigma_m$	Along σ_a since $\sigma_m = 0$	
Determined means of failure if failure is to occur	Fatigue	
Calculated Factor of Safety	1.09487	

* Designing for the worst use case where arm is rotating/turning while being loaded/unloaded.

4.1.3 Analysis of Load Case 2B

In this arm orientation, there is a resultant torsion in the upper arm.

Sketch of Case 2B, is the forearm, elbow and bottom view of upper arm rod (blue) meeting the elbow joint:

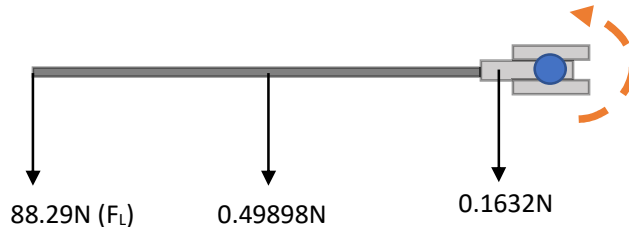


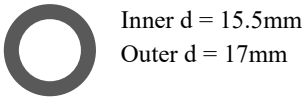
Figure 4.3: FBD and load analysis of applied upper-arm torque in load case 2B

Identified critical location: Surface of the upper arm at shoulder joint (blue dot looking from the bottom), with forearm (grey rod) causing the torque action. Resulting stresses are bending of the upper arm at the shoulder joint and torque

Table 4.5: Static/Yield analysis of upper limb in load case 2B

Critical location		a
Bending moment / Nmm		21400.9
Torque / Nmm		27014.9
Cross-section		 Inner d = 15.5mm Outer d = 17mm
Bending stress / MPa		88.3788
Shear stress / MPa		55.7814
Principal stresses	σ_1 / MPa	148.7
	σ_2 / MPa	60.3208
	σ_3 / MPa	0
Maximum shear stress, τ_{max} / MPa		74.35
Material properties		Mild steel AISI 1020 Ductile $S_y = 395$ MPa
Design Equation		MDET
Calculated Factor of Safety		3.06543

Table 4.6: Fatigue analysis of upper limb in load case 2B

Critical location	a	
Cyclic loading type	Fully reversed	
Bending moment / Nmm	21400.9	
Torque / Nmm	27014.9	
Cross-section		
Bending stress, σ_x / MPa	88.3788	
Mean normal stress: σ_m / MPa	0	
Alternating normal stress: σ_a / MPa	88.3788	
Shear stress, σ_x / MPa	55.7814	
Mean shear stress: σ_m / MPa	0	
Alternating shear stress: σ_a / MPa	55.7814	
Von Misses	σ_m^* / MPa	0
Normal Stresses	σ_a^* / MPa	130.941
Material properties	Mild steel AISI 1020 Ductile $S_y = 395$ MPa $S_{UT} = 470$ MPa	
Specimen Endurance Limit, S_e^* / MPa	235	
Marin Correction Factors	k_a	1.09342 (Cold drawn)
	k_b	0.912886 (Bending and torsion, round, rotating*)
	k_c	1
	k_d	1 (Operation at r.t.p)
	k_e	1 (50% reliability min)
	k_f	1 (No miscellaneous effects)
Endurance strength, S_e / MPa	234.569	
Failure Criterion	Modified Goodman	
S_m	320.275	
S_a	74.7254	
Slope of reference line, $r_c = S_a/S_m$	4.28603	
Slope of load line, $r_L = \sigma_a/\sigma_m$	Along σ_a since $\sigma_m = 0$	
Determined means of failure if failure is to occur	Fatigue	
Calculated Factor of Safety	1.79141	

* Designing for the worst use case where arm is rotating/turning while being loaded/unloaded.

4.1.4 Analysis of Load Case 3C

In this arm orientation, there is a resultant bending and torsion in the shoulder.

Sketch of Case 3C, is the forearm, elbow, upper arm and shoulder:

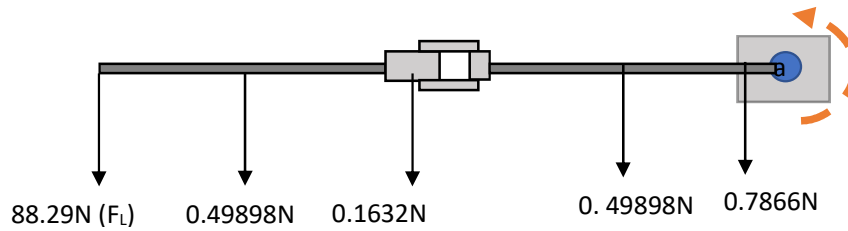


Figure 4.4: FBD and load analysis of applied shoulder torque in load case 3C

Identified critical location: Surface of the shoulder rod at shoulder joint to shoulder socket (blue dot looking from the bottom), with forearm and upper arm (grey) causing the torque action. Resulting stresses are bending of the shoulder rod at the shoulder socket and torque

Table 4.7: Static/Yield analysis of shoulder socket rod in load case 3C

Critical location		a
Bending moment / Nmm		3609.59
Torque / Nmm		59156.5
Cross-section		 Inner d = 15.5mm Outer d = 17mm
Bending stress / MPa		14.9064
Shear stress / MPa		122.148
Principal stresses	σ_1 / MPa	129.828
	σ_2 / MPa	-114.922
	σ_3 / MPa	0
Maximum shear stress, τ_{max} / MPa		122.375
Material properties		Mild steel AISI 1020 Ductile $S_y = 395$ MPa
Design Equation		MDET
Calculated Factor of Safety		1.86243

Table 4.8: Fatigue analysis of shoulder socket rod in load case 3C

Critical location	a	
Cyclic loading type	Fully reversed	
Bending moment / Nmm	3609.59	
Torque / Nmm	59156.5	
Cross-section	 Inner d = 15.5mm Outer d = 17mm	
Bending stress, σ_x / MPa	14.9064	
Mean normal stress: σ_m / MPa	0	
Alternating normal stress: σ_a / MPa	14.9064	
Shear stress, σ_x / MPa	122.148	
Mean shear stress: σ_m / MPa	0	
Alternating shear stress: σ_a / MPa	122.148	
Von Misses	σ_m' / MPa	0
Normal Stresses	σ_a' / MPa	212.091
Material properties	Mild steel AISI 1020 Ductile $S_y = 395$ MPa $S_{UT} = 470$ MPa	
Specimen Endurance Limit, S_e' / MPa	235	
Marin Correction Factors	k_a	1.09342 (Machined/Cold-drawn)
	k_b	0.912886 (Bending and torsion, round, rotating*)
	k_c	1
	k_d	1 (Operation at r.t.p)
	k_e	1 (50% reliability min)
	k_f	1 (No miscellaneous effects)
Endurance strength, S_e / MPa	234.569	
Failure Criterion	Modified Goodman	
S_m	320.275	
S_a	74.7254	
Slope of reference line, $r_c = S_a/S_m$	4.28603	
Slope of load line, $r_L = \sigma_a/\sigma_m$	Along σ_a since $\sigma_m = 0$	
Determined means of failure if failure is to occur	Fatigue	
Calculated Factor of Safety	1.10598	

* Designing for the worst use case where arm is rotating/turning while being loaded/unloaded.

4.1.5 Analysis of Load Case 4B

In this arm orientation, there is a resultant tension at the elbow joint.

Sketch of Case 4B, is the upper section of the elbow in tension:

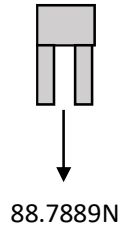


Figure 4.5: FBD and load analysis of upper-elbow joint in load case 4B

Identified critical locations: thin section of elbow joint and thicker section of elbow joint above. Load split at thin section.

Table 4.9: Static/Yield analysis of upper-elbow joint in load case 4B

Critical location	Lower thin section	Upper thick section	
Axial Load / N	44.3945	88.7889	
Cross-section	 h = 30mm b = 10mm	 h = 40mm b = 40mm	
Normal stress / MPa	0.147982	0.055493	
Principal stresses	σ_1 / MPa	0.147982	0.055493
	σ_2 / MPa	0	
	σ_3 / MPa	0	
Material properties	ABS Ductile polymer $S_y \approx 28$ MPa	ABS Ductile polymer $S_y \approx 28$ MPa	
Design Equation	MDET	MDET	
Calculated Factor of Safety	189.212	504.568	

This joint has a highly likelihood of failing by bending as opposed to its extremely safe design under the same dimensions for an axial load. To not compromise its structural integrity during bending, the cross-sectional dimensions are maintained despite the unnecessarily large factor of safety when under axial load.

With unavailable secondary research on the S-N curve for ABS material, the endurance limits of the material cannot be easily determined, as such the part's fatigue analysis would be

performed using SolidWorks to determine the existing fatigue strength and corresponding part factor of safety.

4.1.6 Analysis of Load Case 4D

In this arm orientation, there is a resultant bending in the shoulder rod (blue) to be calculated. Sketch of Case 4D, is shoulder rod (blue), shoulder, upper arm to forearm at the given arm orientation:

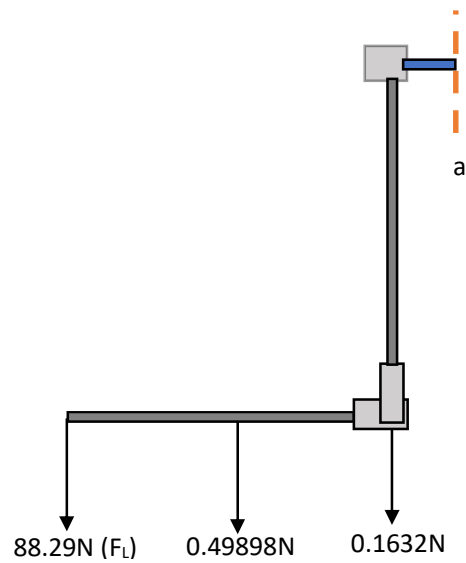


Figure 4.6: FBD and load analysis of shoulder in load case 4D

Identified critical location: at a where the rod is held fixed in the socket

The effective bending is performed at the shoulder by the load transmitted through the upper arm rod, thus all loads are summed.

Table 4.10: Static/Yield analysis of shoulder socket rod in load case 4D

Critical location	a
Bending moment / Nmm	3609.59
Cross-section	 Inner d = 15mm Outer d = 17.5mm

Bending stress / MPa		14.9064
Principal stresses	σ_1 / MPa	14.9064
	σ_2 / MPa	0
	σ_3 / MPa	0
Material properties		Mild steel AISI 1020 Cold drawn Ductile $S_y = 395$ MPa
Design Equation		MDET
Calculated Factor of Safety		26.4987

Table 4.11: Fatigue analysis of shoulder socket rod in load case 4D

Critical location		a
Cyclic loading type		Fully reversed
Bending moment / Nmm		3609.59
Cross-section		 Inner d = 15mm Outer d = 17.5mm
Bending stress, σ_x / MPa		14.9064
Mean: σ_m / MPa		0
Alternating: σ_a / MPa		14.9064
Von Misses	σ_m' / MPa	0
Normal Stresses	σ_a' / MPa	14.9064
Material properties		Mild steel AISI 1020 Ductile $S_y = 395$ MPa $S_{UT} = 470$ MPa
Specimen Endurance Limit, S_e' / MPa		235
Marin Correction Factors	k_a	1.09342 (Cold drawn)
	k_b	0.912886 (Bending, round, rotating*)
	k_c	1 (bending)
	k_d	1 (Operation at r.t.p)
	k_e	1 (50% reliability min)
	k_f	1 (No miscellaneous effects)
Endurance strength, S_e / MPa		234.569
Failure Criterion		Modified Goodman
S_m		320.275
S_a		74.7254
Slope of reference line, $r_c = S_a/S_m$		4.28603
Slope of load line, $r_L = \sigma_a/\sigma_m$		Along σ_a since $\sigma_m = 0$
Determined means of failure if failure is to occur		Fatigue
Calculated Factor of Safety		15.765

** Designing for the worst use case where arm is rotating/turning while being loaded/unloaded.

Despite the unnecessarily high factor of safety in this load scenario, the shoulder experiences drastically higher stresses during high torsional orientations, and as such the factor of safety is lower in those cases and used in determining the sizing and thresholds instead.

4.1.7 Analysis of Load Case 5E

In this arm orientation, there is a resultant tension at the elbow joint.

Sketch of Case 4B, is the lower part of the elbow connecting to the forearm in tension:

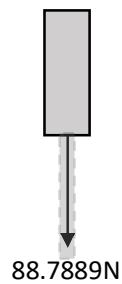


Figure 4.7: FBD and load analysis of lower-elbow joint in load case 5E

Identified critical locations: this section of elbow joint and thicker section of elbow joint above. Assuming fixed at o. Load split at thin section.

Table 4.12: Static/Yield analysis of lower-elbow joint in load case 5E

Critical location		Lower thin section
Axial Load / N		88.7889
Cross-section		 $h = 30\text{mm}$ $b = 30\text{mm}$
Normal stress / MPa		0.098654
Principal stresses	σ_1 / MPa	0.098654
	σ_2 / MPa	0
	σ_3 / MPa	0
Material properties		ABS Ductile polymer $S_y \approx 28 \text{ MPa}$
Design Equation		MDET
Calculated Factor of Safety		283.819

Similar to case 4B, this joint has a highly likelihood of failing by bending as opposed to its extremely safe axial loading design under the same dimensions. Thus, to no result in failure the dimensions are maintained so as to not compromise its safety against the bending stresses during operation.

As with case 4B, unavailable secondary research on the S-N curve for ABS material, led to the performance of the joint's fatigue analysis in SolidWorks instead.

4.2 Numerical Analysis

Mechanical Analysis is performed by running Finite Element Simulation in SolidWorks, the fatigue charts utilised in the models were autogenerated in SolidWorks, based on the material decisions made in the design chapter. For the fatigue analysis of ABS, and approximate S-N chart (Appendix A) based on is utilized in the simulated fatigue stress analysis.

4.2.1 Identified key stress components

The primary loaded parts are:

- The wrist
- The limb rods
- The elbow
- The shoulder
- The shoulder support rods
- The shoulder support socket
- The double-cardan joint

However, this subsection delves into the analysis of the complex components of which their design safety has not yet been assessed analytically. Consequently, this means a

focus on the wrist, the shoulder, the shoulder support rods, the shoulder support socket, and the double cardan joint.

4.2.2 Stress analysis of shoulder rod under Operational Load Scenario 3C

With the rod fixed into the double cardan joint and supported on the opposite end by a fixed bearing, the expected total force exerted on the shoulder pulley for shoulder flexion/extension is transferred to the rod and analysed.

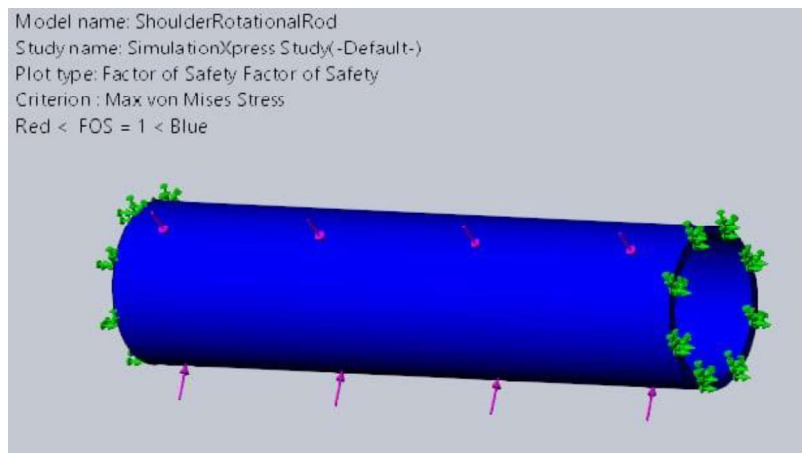


Figure 4.8: F.O.S contour results for loaded shoulder rod at shoulder pulley unit

Table 4.13: Shoulder pulley rod bearing muscle force results

Von Mises Maximum Stresses	$4.325 \times 10^6 \text{ Nm}^{-2}$
Maximum deflection	0.0001436 mm

Based on the design and chosen AISI 1020 material the expected factor of safety by mean of normally loading the surface is 81.2839.

In checking for the torsional stresses, the calculated torque of 59156.5Nmm, driven by the pulley through the arms weight and muscle support is applied to the rod. At load case 3C this is the arm orientation to drive the largest torque and put the largest strain on the arm.

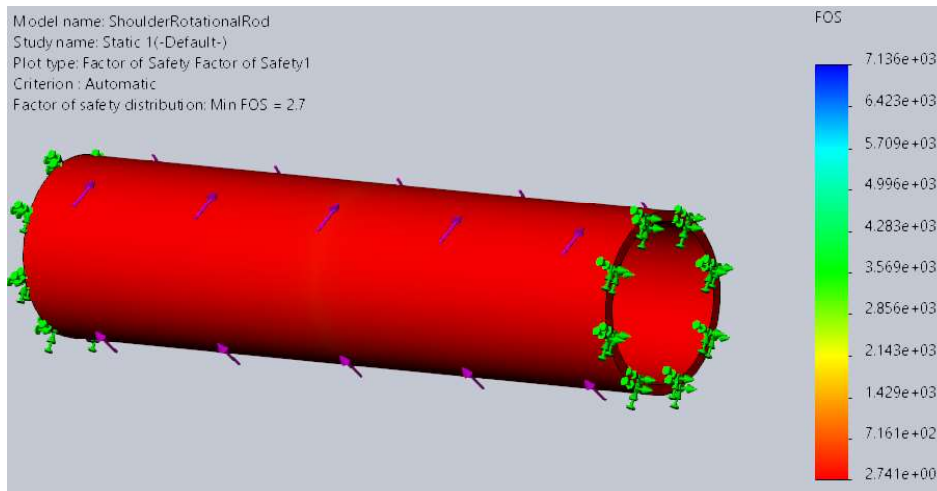


Figure 4.9: F.O.S result for torsional stress in shoulder rod at shoulder pulley unit

Table 4.14: Shoulder pulley rod torsional results

Von Mises Maximum Stresses	$1.283 \times 10^8 \text{ Nm}^{-2}$
Maximum displacement	0.01651 mm
Minimum F.O.S	2.7

Of similar value range to the analytical calculation even in this worst-case loading scenario, the shoulder rod offers a 2.7 factor of safety.

With evident likely failure by the torsional load, a fatigue analysis is performed on this load type, to determine any possible fatigue failures. SolidWorks indicates no damage as the part was designed for infinite life cycle and the alternating stresses, σ_a is a factor below the endurance strength and as such safe and would show now damage or limited life cycle through the simulation as desired.

4.2.3 Stress analysis of shoulder socket rod under Load Scenario 3C, 4D & 5E

Under each of these load scenarios the rod experiences bending from being loaded on the arm end and held fixed in the shoulder socket, and in the case of 3C there is an acting torque as calculated in the shoulder rode driven by the pulley.

The calculated bending moment applied on the rod is 3609.59 Nmm.

By effecting a split line on the rod, the load can be applied on the region of the rod that is held within the shoulder joint.

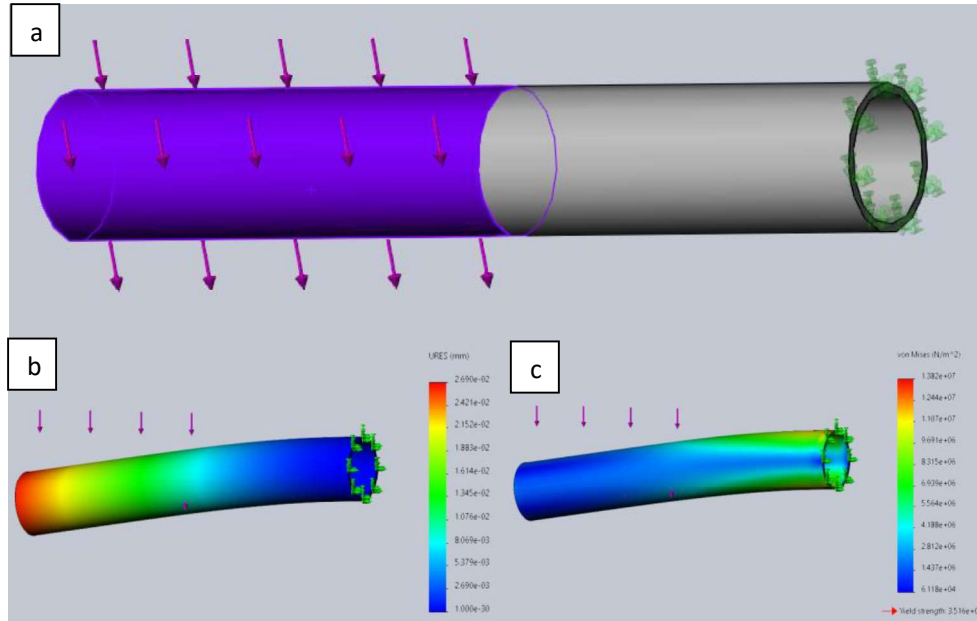


Figure 4.10: Simulation results for shoulder socket rod under bending load; (a) Applied load region, (b) Deflection/deformation result, (c) von Mises stress result from bending load

Table 4.15: Shoulder socket rod bearing arm load results

Von Mises Maximum Stresses	$1.382 \times 10^7 \text{ Nm}^{-2}$
Maximum displacement	0.0269 mm
Minimum F.O.S	25.44

There is a near negligible bending of the rod at the highest possible load for the arm. The maximum displacement is 0.0269 mm of which is far less than a visible millimetre.

Under these load conditions the minimum factor of safety for the rod is 25.44, as the bending moment effected on this short rod is lower than the torsional load expected during arm flexion/extension.

Under case 3C this component experiences a torque of 59156.5Nmm (59.1565Nm).

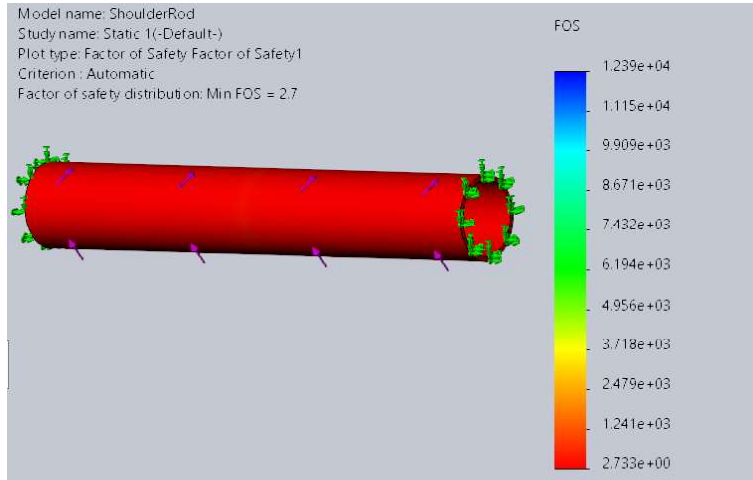


Figure 4.11: F.O.S result for torsional stress in shoulder socket rod

Table 4.16: Shoulder socket rod torsional results

Von Mises Maximum Stresses	$1.286 \times 10^8 \text{ Nm}^{-2}$
Maximum displacement	0.02595 mm
Minimum F.O.S	2.733

An ideal factor of safety of 2.733 is obtained from the static load assessment of torsional stress on the rod, meeting our design specific range for safety.

As with the shoulder rod bearing the pulley, the rod design for infinite life has an alternating stress a factor below the endurance strength of the AISI 1020 rod, as such would not fail under cyclic loading for an infinite cycle. This factor below the fatigue strength is calculated in the load analysis of case 4D and 3C.

4.2.4 Stress analysis of shoulder under all Operational Load Scenario

The shoulder component experiences at least 3 defined load types and orientations. Holding the internal section of the shoulder in which the shoulder rod remains fixed, the lower shoulder plate of which leads to the contact point of the upper arm is loaded in all 3 axis directions and applied moments.

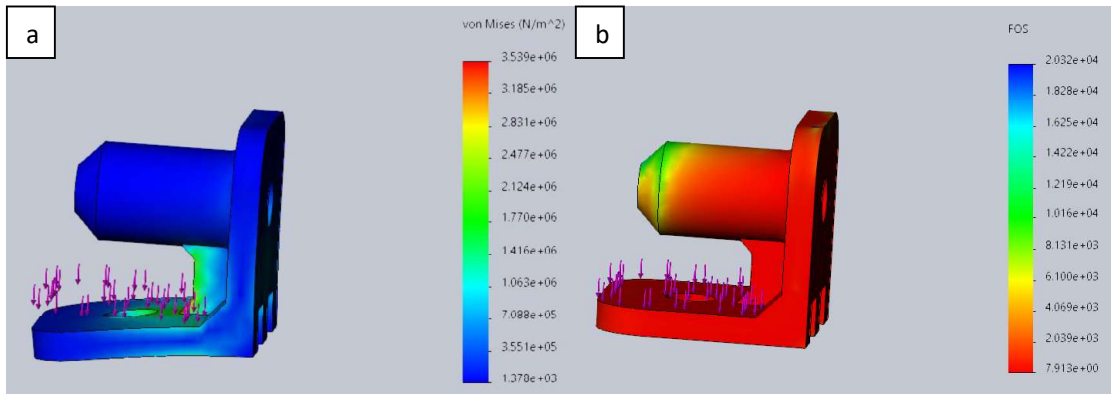


Figure 4.12: Simulation results for shoulder as connecting upper arm is axially loaded; (a) von Mises stress result as plate of shoulder to upper arm is loaded down, (b) F.O.S result

Table 4.17: Shoulder vertically adducted bearing arm load results

Von Mises Maximum Stresses	$3.539 \times 10^6 \text{ Nm}^{-2}$
Maximum displacement	0.02595 mm
Minimum F.O.S	7.913

With a minimum factor of safety of 7.913, the shoulder joint offers safe operability under the axial load of the arm, however in its 3D-printing production, the porosity and layering of the print material on the component would reduce the evident factor of safety of the component by up to $\frac{1}{4}$ its value [38]. As such 7.913 is not a likely over design with the component being manufactured attaining a factor of safety value of approximately 2.63767 compared to a solid ABS component. This is applied to subsequent ABS components.

Fatigue analysis of this load scenario and the load scenarios, 1B and 3C, assessed blow, on this part indicated no failure by fatigue, as alternating stresses are well below the fatigue strength of ABS provided.

Oriented as in load case 1B the upper arm exerts a bearing load within its socket on the shoulder. A static load analysis of this loading, with an upper arm weight of 90.2378N results in:

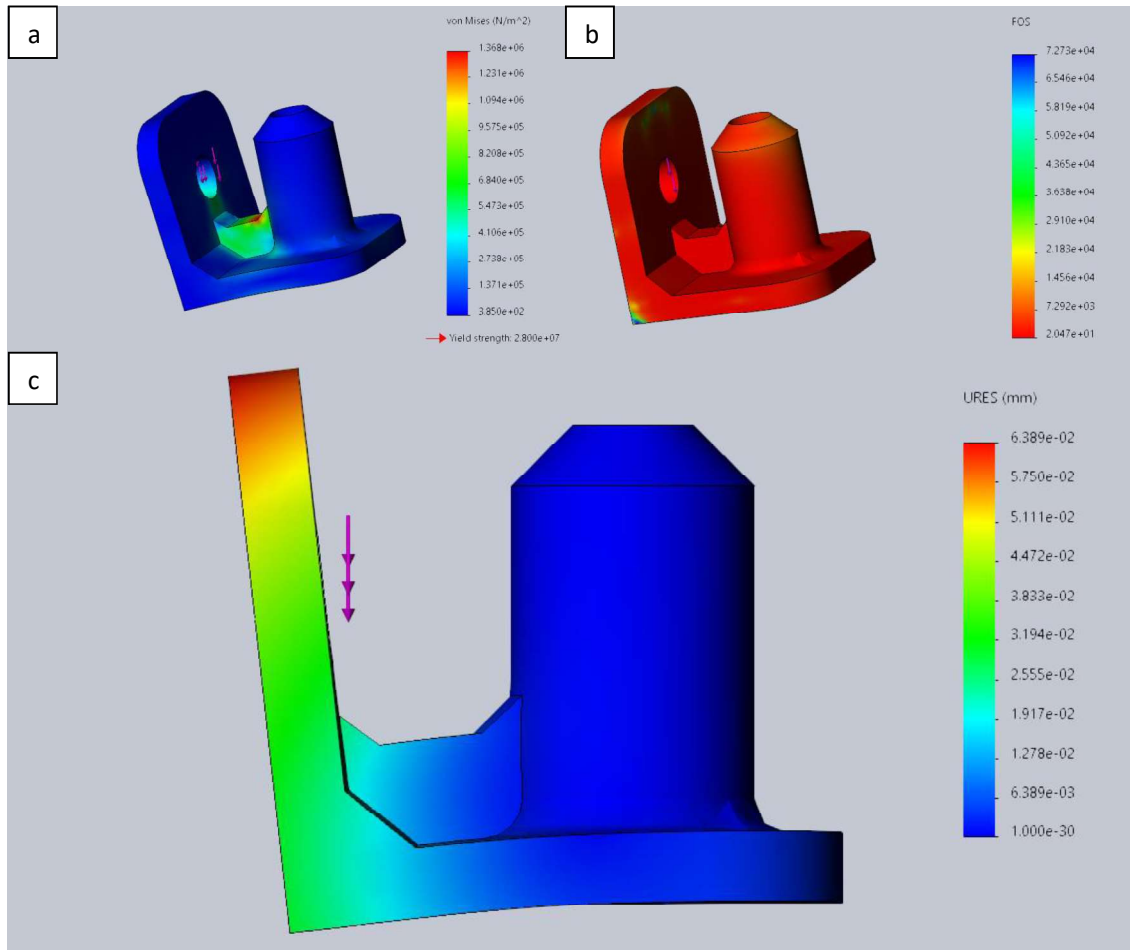


Figure 4.13: Simulation results for shoulder as upper arm is horizontally abducted; (a) von Mises stress result as plate of shoulder to upper arm is laterally loaded when elevated, (b) F.O.S result, (c) Displacement/deflection result

Table 4.18: Shoulder horizontally abducted (elevated) bearing arm load results

Von Mises Maximum Stresses	$1.368 \times 10^6 \text{ Nm}^{-2}$
Maximum displacement	0.06389 mm
Minimum F.O.S	20.47

In the case of 3C, in which the arm is in flexion/extension at its largest torque position, the direction of the arm weight on the upper arm is changed to the y-axis of the component and as such produce these stress results:

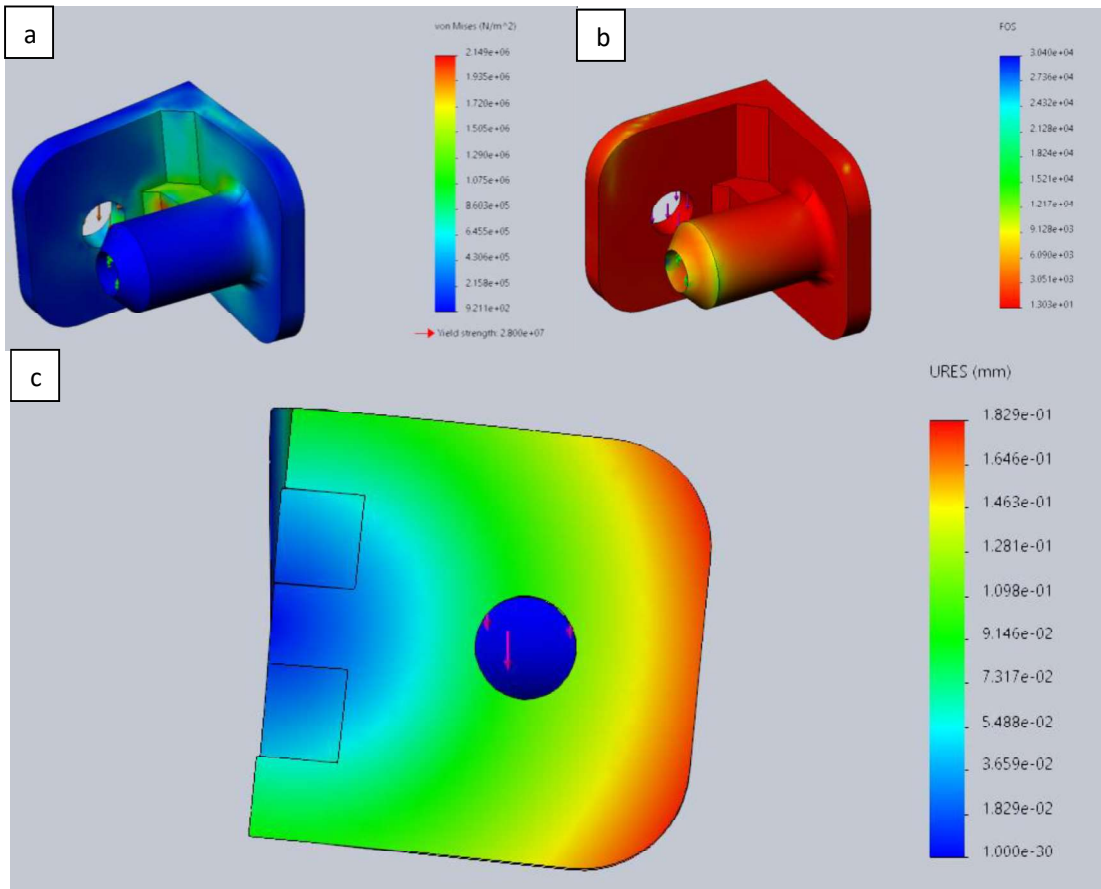


Figure 4.14: Simulation results for shoulder as shoulder is in horizontal extension; (a) von Mises stress result as plate of shoulder to upper arm is laterally loaded during extension, (b) F.O.S result, (c) Displacement/deflection result

Table 4.19: Shoulder horizontally flexed/extended bearing arm load results

Von Mises Maximum Stresses	$2.149 \times 10^6 \text{ Nm}^{-2}$
Maximum displacement	0.1829 mm
Minimum F.O.S	13.03

The introduced flange between the shoulder rod socket and the upper arm's contact plate, as well as the flanged sections at the 90° bend, assist in reducing stress concentrations within the shoulder.

The least factor of safety for the shoulder component being 7.913 when the upper arm joint is loaded axially, and the bearing plate normally loads the shoulder's lower plate.

4.2.5 Stress analysis of wrist under Bending and Axial Operational Load Scenarios

The wrist joint, oriented as in the end effector of load case of 2B and 3C, would experience bending of which would not be translated directly into the muscle support but would rather be borne by the structure due to the 1 D.O.F in this design. As such the stresses under bending and in direct axial loading in supporting 88.29N is simulated and assessed.

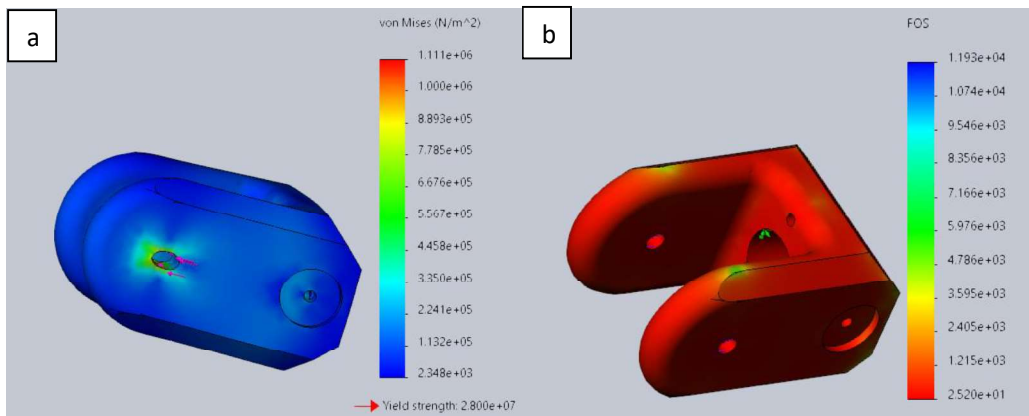


Figure 4.15: Simulation results for wrist joint as wrist receptor is axially loaded; (a) von Mises stress result, (b) F.O.S result

Table 4.20: Wrist joint axially loaded results

Von Mises Maximum Stresses	$1.111 \times 10^6 \text{ Nm}^{-2}$
Maximum displacement	0.01065 mm
Minimum F.O.S	25.20

When the wrist is loaded in the action to bend the joint, these are the simulated results in either bent directions.

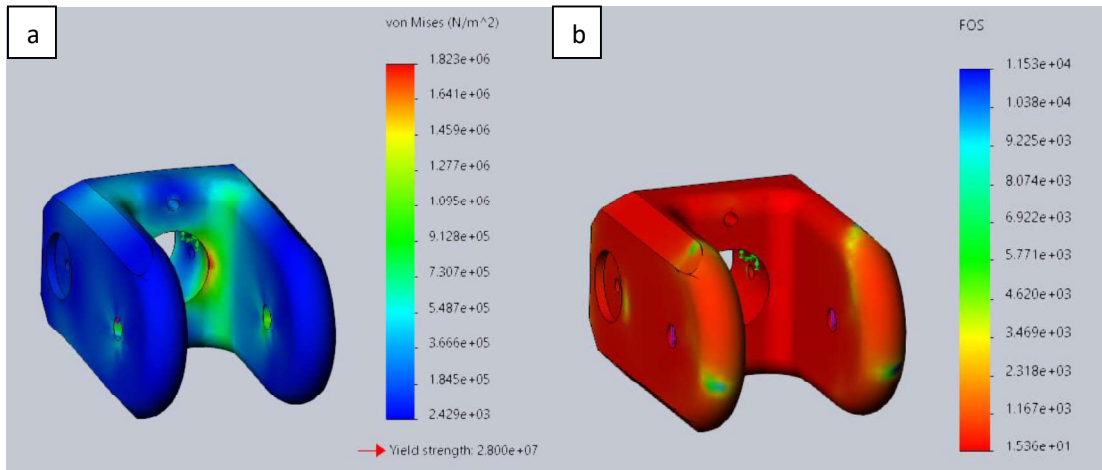


Figure 4.16: Simulation results for wrist joint as wrist receptor is laterally loaded; (a) von Mises stress result, (b) F.O.S result

Table 4.21: Wrist joint laterally loaded results

Von Mises Maximum Stresses	$1.823 \times 10^6 \text{ Nm}^{-2}$
Maximum displacement	0.03239 mm
Minimum F.O.S	15.36

4.2.6 Stress analysis of shoulder socket under Operational Load Scenario 1C & 3C

About the mentioned load locations, the arm creates a downward bearing load of 90.2378N within the socket with the rotational joint fixed (fixed hinge), this would transmit the bearing load into torsion at load case 1C.

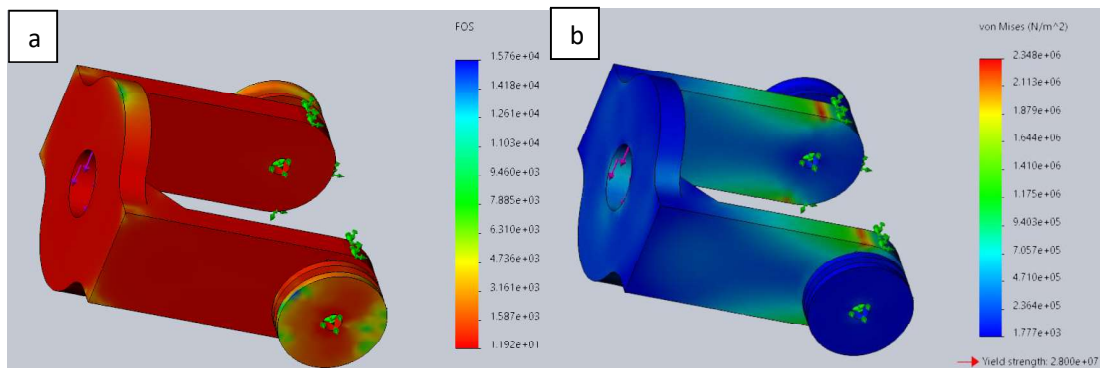


Figure 4.17: Simulation results for shoulder socket as shoulder rod at maximum bending; (a) von Mises stress result, (b) F.O.S result

Table 4.22: Shoulder socket maximum torsional elevation results

Von Mises Maximum Stresses	$2.348 \times 10^6 \text{ Nm}^{-2}$
Maximum displacement	0.1218 mm
Minimum F.O.S	11.92

4.2.7 Stress analysis of double cardan joint under Operational Load Scenario 3C

The high stress effect in the shoulder joint during flexion/extension is propagated as a torsional stress into the double cardan joint connecting the respective shoulder rods. On one end the male yoke from the shoulder socket rod is driven by a torque at the end and held fixed at the joint's cross connection to the female yoke. This is load effect is assessed for one male yoke as it is replicated on the other end. The female yoke between each male yoke is likewise loaded in similar manner with its cross joint fixed and a torque applied to its circumference. Lastly the connecting rod/shaft of which allows the joint to extend and contract as a centring mechanism is applied the same torque. The walls of the yokes are of plain carbon steel which form an encasement around the 3D-printed element of the joint (for model testing). Of final design, a standardized double cardan joint with a centring mechanism is advised for its higher strength and much more accurate performance.

The different components within the double cardan joint (male yokes, female yokes, cross linkage and extension shaft) are analysed and the least safe component (the short extension shaft designed to be made from plain carbon steel just as the rest of the joint) is presented in Figure 4.18.

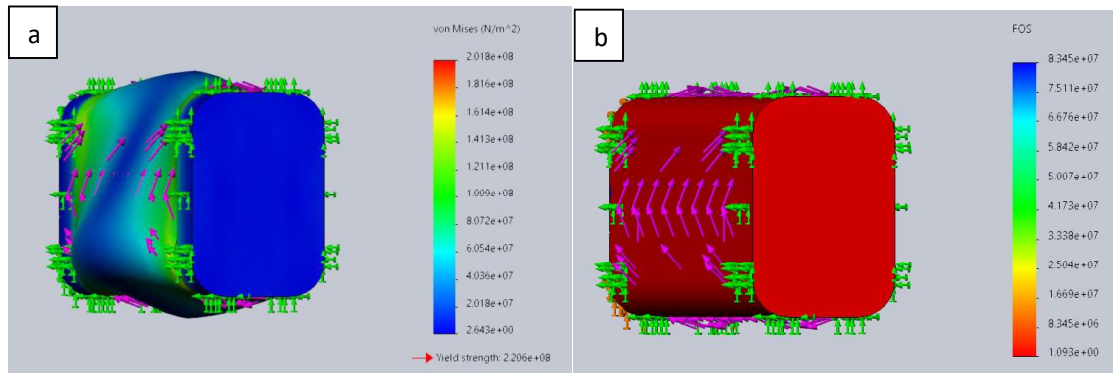


Figure 4.18: Simulation results for components of double cardan joint during torsion;
 (a) von Mises stress result, (b) F.O.S result

Table 4.23: Double cardan shaft torsional results

Von Mises Maximum Stresses	$2.018 \times 10^8 \text{ Nm}^{-2}$
Maximum displacement	0.007468 mm
Minimum F.O.S	1.093

4.3 Muscle Fabrication and Experimental Analysis

Based on the total force calculations and required muscle extensions, from the model design in Chapter 3.4-3.5, the muscles are fabricated as large muscles for larger force production and extensions, and small muscles for smaller force production and finer smaller extensions.

The large muscles are designed to operate the larger torsional load scenarios and as such from the calculated torsional and bending stresses, are situated on the upper arm and in the chest support. Operation of the wrist is performed using the smaller sized muscles.

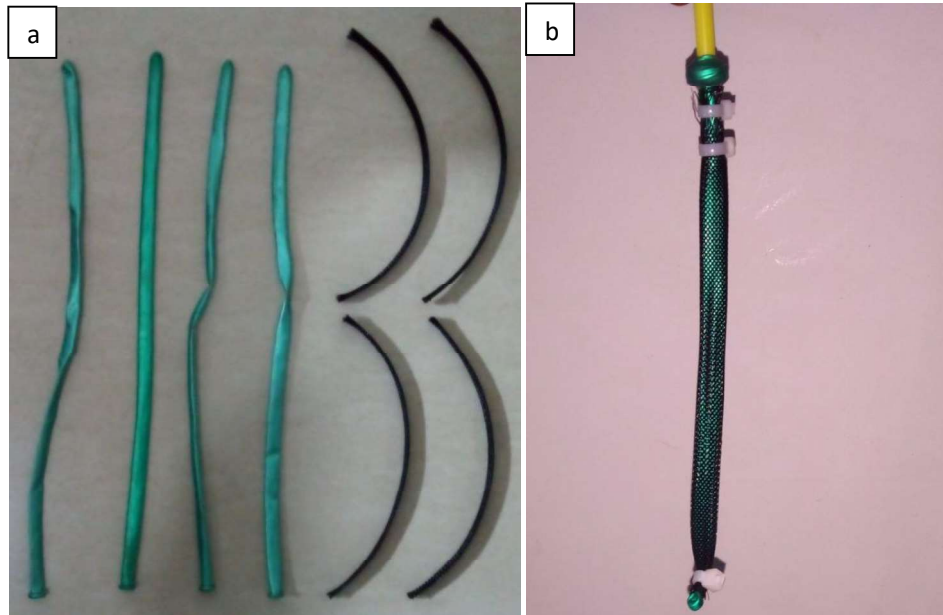


Figure 4.19: Fabrication of McKibben muscles; (a) latex tubes and braided sleeving, (b) Complete muscle with sleeving fixed with zip-ties and pressure feed-in tube (yellow).

The muscles are created by inserting the latex tubes at unstretched length into the braided sleeving (Figure 4.9). The sleeving is attached to the inner latex tube of the muscle by zip-ties. A hard plastic tube is fed and held in place with the upper two zip-ties holding the sleeve and the tube. This helps keep an airtight seal in addition to the rubber's tight elastic end. The effective length recorded in Table 3.15 of the muscle is then the distance between the lower end zip-tie and the lower zip-tie on the muscle's inlet/outlet.

To test and validate the theoretical sigmoidal functions used in estimating the muscle performance (expansions against force) under a given pressure, the theoretical data is compared against an experimental analysis of the muscles. The muscles are each attached to a spring of known spring constant and length. The muscle is then pressurized to a set point (50kPa is used for this safe testing). The pressurized muscle is then attached to the spring and used to draw down the spring to various set lengths. The resulting spring extension is used to determine the force loaded on the muscle, and the length of the muscle is calculated against its original length to determine the muscle contraction under that given force and pressure. This is experiment is

repeated (Test T1-T7) at each pressure-force point for the two muscle sizes and seeks to validate the muscle performance theoretically estimated. Experimental data is provided in Appendix C.

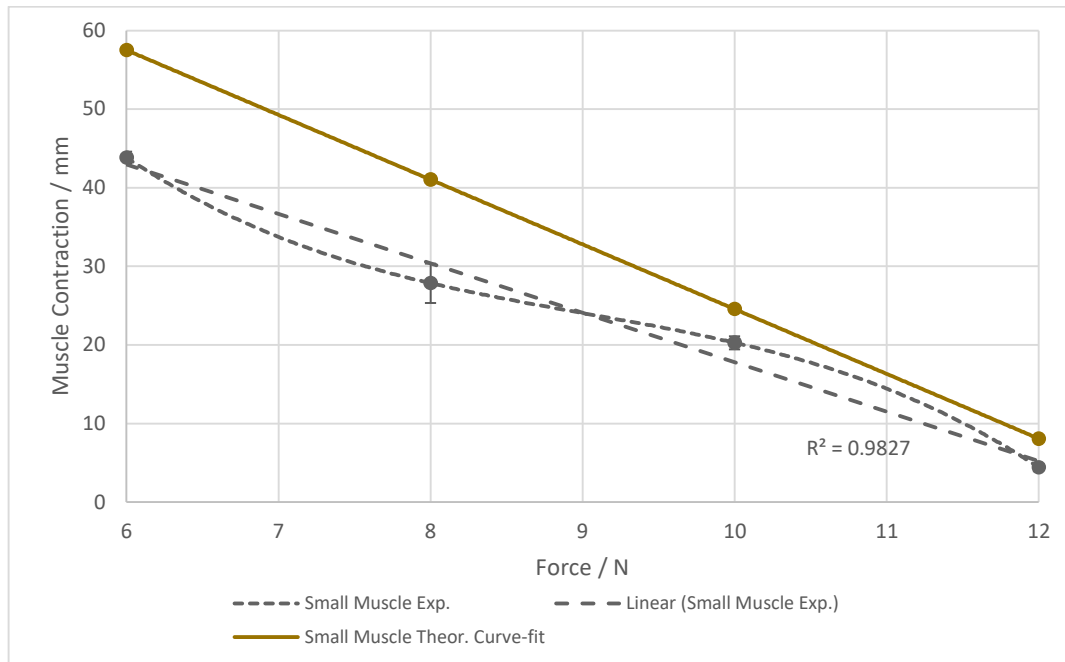


Figure 4.20: Plot of small muscle load-contraction under 50 kPa test pressure; Error bars are 1 standard deviation of experimental data. Curve fits are power of 3 polynomials, with a linear fit tested.

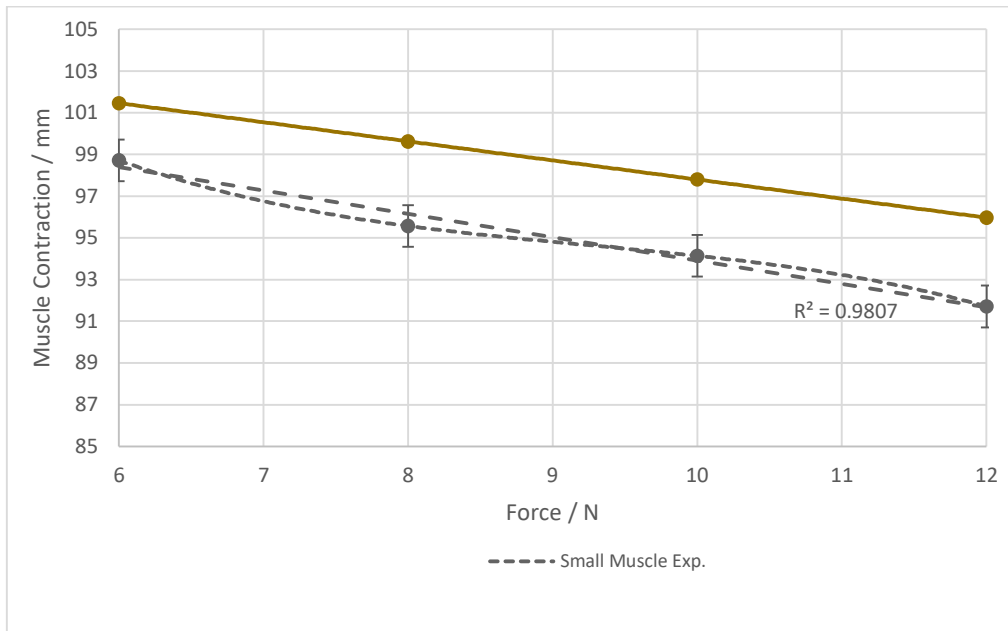


Figure 4.21: Plot of large muscle load-contraction under 50 kPa test pressure; Error bars are 1 standard deviation of experimental data. Curve fits are power of 3 polynomials, with a linear fit tested.

The demonstrated muscle model displays similar performance characteristics between the experimental results and the theoretical estimates. The deviation in muscle extension, is due to the latex tubing used. The theoretical model assumes a near negligible tubing thickness, and as such its elastic properties is theoretically assumed to be negligible in the model suggested. However, in practicality, the latex material still offers a degree of elasticity after pressurization, and as such the loaded force is still able to pull on the muscle and prevent it from reaching its full theoretical expansion under the given pressure and load. This amounts for the 23.8% maximum deviation error from the theoretical contraction for the small muscle, and 4.4% for that of the large muscle.

Nonetheless, despite's the McKibben's non-linear relationship between pressure and extension, for a fixed pressure, it displays mechanical performance of which can be near linearly approximated with an R^2 value of 0.9824 for the smaller muscle and 0.9807 for the larger muscle, both of which indicate a close 98% goodness of fit for this data approximation.

Chapter 5: Implementation

This chapter outlines the fabrication of the arm based on the thorough designs produced and simulations performed. Skeletal structure is tested for the fluidity of actual joint motion and its realized D.O.F as compared to the simulated motion analysis. The arm is fully assembled, and individual muscles tested for operation.

5.1 Skeletal structure fabrication

5.1.1 Arm fabrication

The arm joints were 3D printed from ABS as design specified, and the limb rods were cut from mild steel tubes based on the material specifications designed with. Joining of the rod to the arm joints were made using both epoxy and tapping screws.



Figure 5.1: 3D-printed lightweight arm joint components

The chest supporting frame is identified as a non-design essential component as the arm can be bolted and screwed onto any surface with its intended installation point being the shoulder girdle of a humanoid robot. As such the chest support was cut and welded to form from galvanized steel for low weight during transporting of the arm around and for its strength properties in forming a sturdy clampable structure.



Figure 5.2: Sheet metal cutting of humanoid arm shoulder support and limbs

To also leverage the light-weighted design, the bearings utilised in the model were held modelled in place by a folded 0.5mm thick steel sheet. These were fabricated from cut steel strips and attached to the bearing using epoxy steel to make a lighter, equally strong, bearing housing than the heavier weight solid steel block housings/bed.

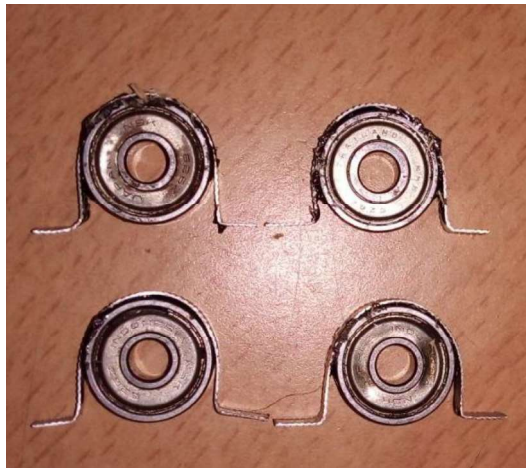


Figure 5.3: Bearing housed in stainless steel metal strips adhered with epoxy steel

The cross joint (Figure 5.3) within the double cardan joints were carved and hand-drilled from wood and fixed in place using tapping screws so as the joint can be readily assembled and disassembled.

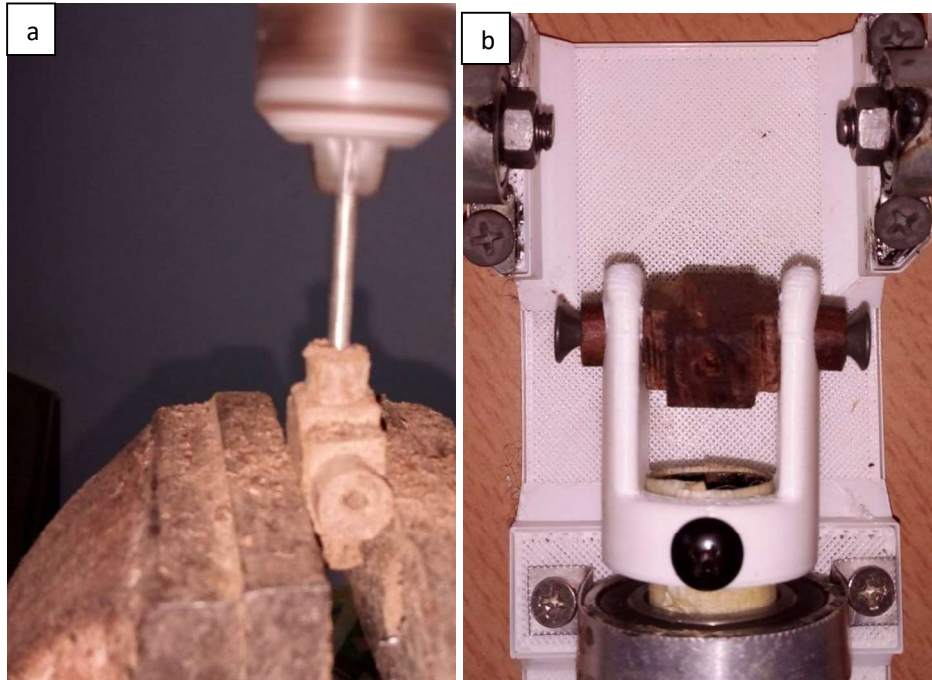


Figure 5.4: Fabrication of cross-linkage for connecting the double cardan joint yokes; (a) Drilling and carving cross-linkage, (b) Assembled and locked cross-linkage on male yoke

5.1.2 Resulting arm assembly

The final jointed unit of the arm assembly is shown below with the upper arm resting on the table and the forearm extending from the elbow upwards. Each fabricated bearing to act as the muscle contact points are adhered and screwed into the joints at its designed locations.



Figure 5.5: Fully jointed arm skeletal unit

5.1.3 Resulting shoulder assembly

The shoulder unit was assembled as designed and the extensor connection of the double cardan joint slightly greased and tested for fluidity in motion.

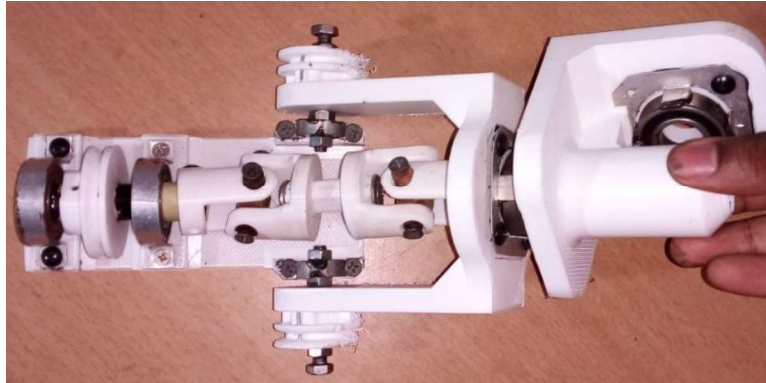


Figure 5.6: Assembled shoulder module top view with shoulder tilted in extension; (From left to right) Shoulder supporting bearings, Shoulder flexion/extension pulley on shoulder, Double cardan joint, Shoulder abduction/adduction socket, Shoulder



Figure 5.7: Assembled shoulder module side view with shoulder in abduction (elevated); (From left to right) Shoulder supporting bearings, Shoulder flexion/extension pulley on shoulder, Double cardan joint, Shoulder abduction/adduction socket, Shoulder

Figure 5.6 & 5.7, demonstrate the working principle of the double cardan joint in realization, as the shoulder flexion/extension pulley system remains level and fixed on the shoulder base but still transfers the driving torque to the shoulder through the cantered double

cardan joint despite its angle of elevation. Alignment of the double cardan joint is made possible by aligning the bearing axis for shoulder elevation directly with the midplane of the joint from end face to end face in horizontal position. This, as designed, ensures in elevation, each cardan joint (on at the shoulder pulley rod and the other at the shoulder socket rod) tilt by equal angles in the opposite direction. This ensures the rotational speed and angular displacement of the output rod is in phase and in constant velocity as the input. Using a single joint result in a phase shift and as such the double cardan joint negates this phase shift as presented in the study of the joint [39].

5.2 Muscle assembly

The muscles fabricated by design specifications in Figure 4.19 are attached to the skeletal frame of the arm at the respective freely turning bearings. Each muscle is split into a pair using a Y-joint pressure tube connector.



Figure 5.8: A muscle connection to joint pulley system (forearm wrist joint example)

The muscles are then connected to the pulley joint by a tied monofilament UHMWPE fibre of which has zero stretch for the purpose of this project and have up to four times the strength of nylon for the same 1mm diameter.

The design allows for the muscles to be easily replaceable in cases of a rupture, or any other wear or failure in muscle integrity. The push-in fitting of the Y-joint pressure tube connector means any muscle can be released and removed when needed.

5.3 Complete musculoskeletal assembly

The arm's complete assembly is shown in Figure 5.9, with key muscle components and skeletal parts labelled in Figure 5.10. The humanoid arm houses its battery system and miniature high-pressure pump within the chest support directly below the shoulder support joint of the arm. The shoulder abduction/adduction antagonistic pair and the shoulder flexion/extension antagonistic pair are fixed to the base bearings within the shoulder support (chest cavity) and tied to the UHMWPE fibre as demonstrated for the wrist (Figure 5.8), leading to their respective pulley joints.

The pressure delivery tubes are flexible and loosely bound along the skeleton of the arm of which are strategically ensured to not obstruct the degrees of motion the arm. The muscle valve system and included microcontroller or circuitry can be safely housed within the chest support.

Detailed view of the musculoskeletal system its pulley joint attachments and its attachment to the arm's skeleton are attached in the appendix.

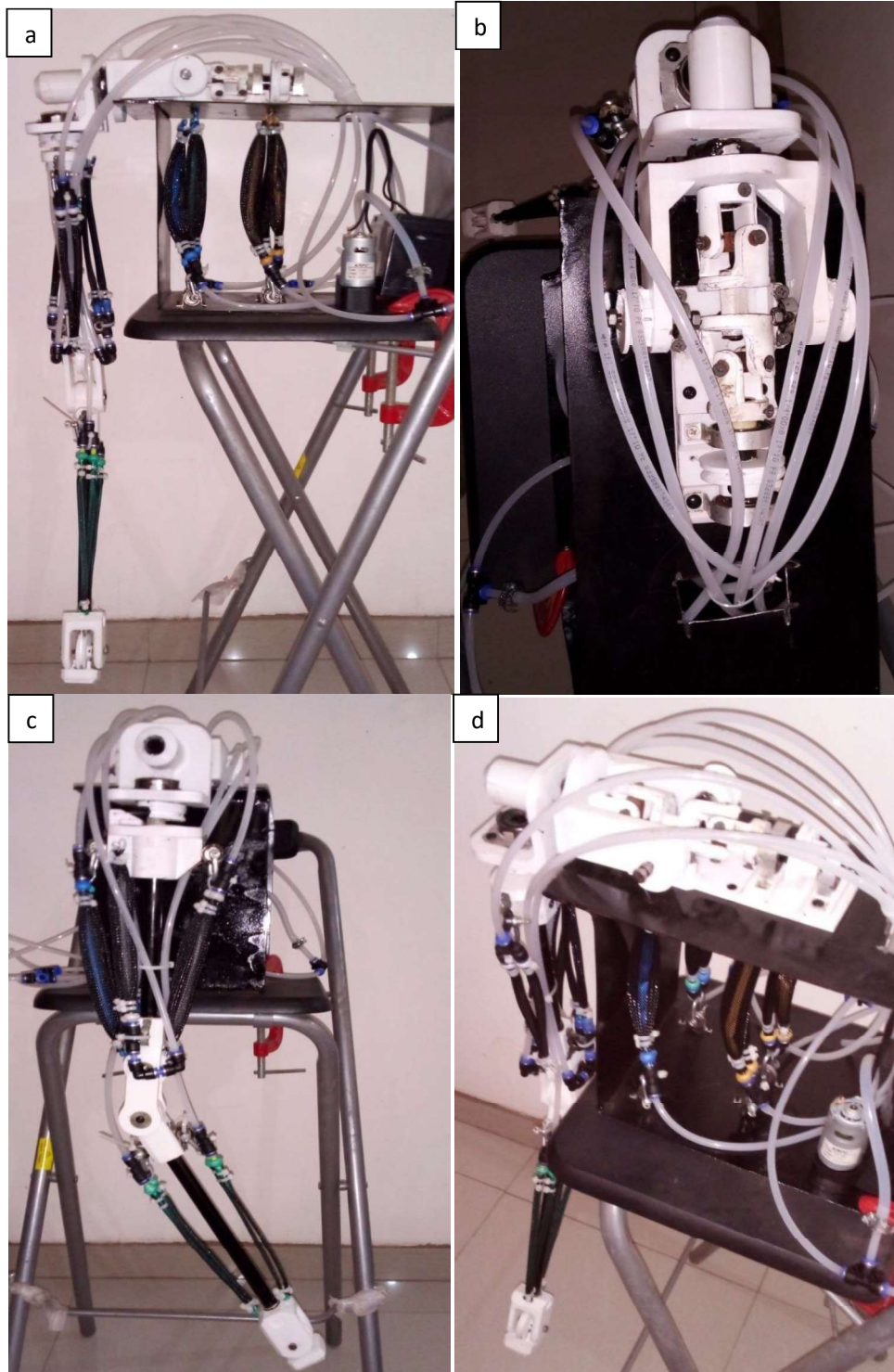


Figure 5.9: Complete modularized arm with muscle and auxiliary units connected; (a) Front view, (b) Top view, (c) Left view, (d) Isometric view

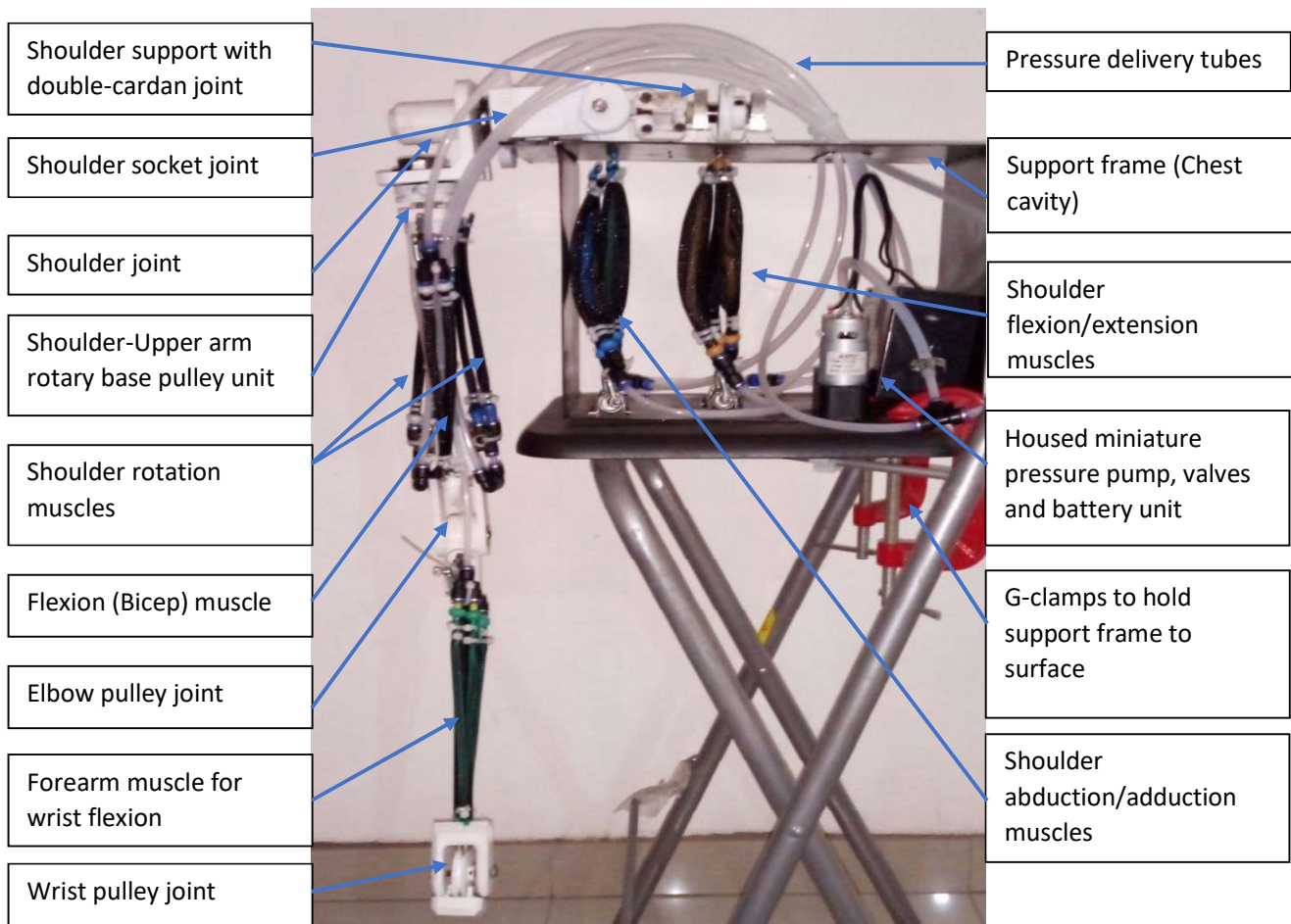


Figure 5.10: Full musculoskeletal system of humanoid arm with labelled parts

5.4 Pressure control schematic and implementation of pump system

The pressure control system for the humanoid arm is described and proposed in Figure 5.10. The system utilizes a proportional valve for each degree of freedom, to regulate actuator speed by controlling flow rate and pressure. This regulated feed is then relayed to the respective sides of each muscle antagonistic pair (within dashed box) that enables the actuation of that degree of freedom. The pressure feed and balancing of the antagonistic pair is handled by the 5/3-way solenoid valve which allows each muscle a single tube feed that can both pressurize and depressurize. The 5/3-way solenoid valve enables a single pressure inlet (1) and a pressurizing of either muscle in the antagonistic pair (through port 2 or 4) while exhausting the

other (through port 3 or 5). The deactivation of the valve maintains the pressure of both muscle units at any point of time and stops the pressurization and depressurization of either muscle.

With the designed system the entire humanoid arm's muscle system can be actuated by a single miniature pump of which has reduced need for continuous pressurization and pressure holding, due to the networked valve action. The humanoid arm designed has a total of 20 McKibben tubing. Each muscle within an antagonistic pair comprises of 2 McKibben tubing.

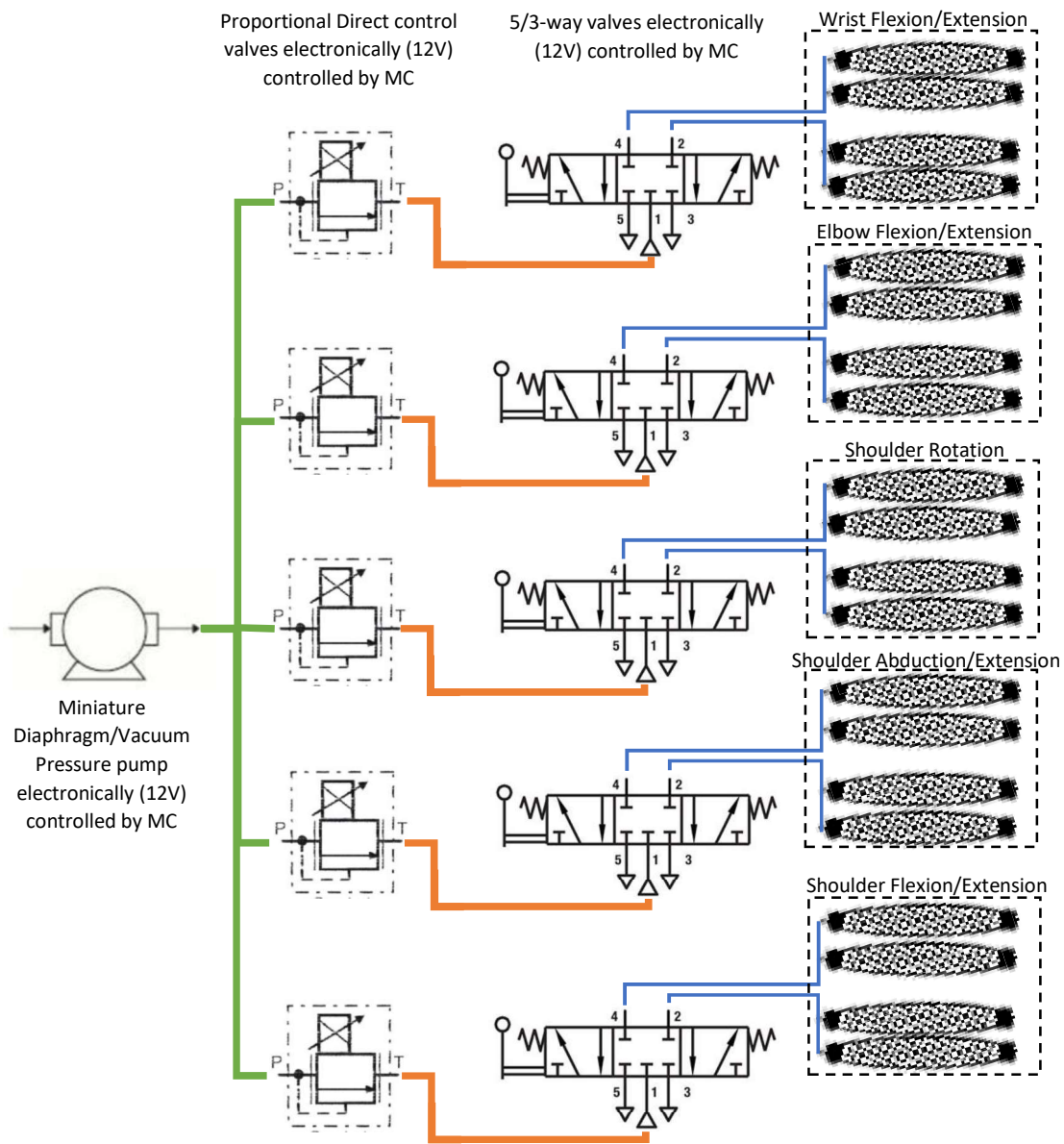


Figure 5.11: Schematic of proposed pressure control valve and pump system

5.4 Arm power performance testing

For arm output power estimation, the arm is pressurized at maximum input power and mechanically tested in its ability to drive a load up a height. To estimate the maximum power that can be transmitted to the load, the test is carried out using the forearm muscles, as these muscles more directly drive the end load as opposed to the other muscles which would incur a considerable power loss for the same power input in having to drive the end load in addition to the arm's own weight/inertia.

The wrist joint is actuated by contracting the upper forearm muscle to cause a rise in the height of the end load. The maximum power is then estimated by the rate of change in potential energy of the given load (test mass 1kg), and this resulting maximum power output rating is appended to Table 6.3.

Chapter 6: Results and Discussions

This chapter curates all design, analysis and performance results for the overall characteristics of the am. These are matched against the design goals and evaluation criteria of the arm.

6.1 Results

The results are subdivided into two categories: mechanical design results summary and actuation performance results summary.

6.1.1 Mechanical design results summary

Assessing each primary stress component by both analytical and numerical means, the table summarizes the results for the least factor of safety for the designed parts and the load means that induces these results. 1.09487

Table 6.1: Critical mechanical analysis results for primary parts

Primary Component	Factor of safety	Load description
Forearm limb	2.37604	Resulting fatigue during bending under maximum load in repeated operation while rotating
Upper arm limb	1.09487	Resulting fatigue during bending under maximum load in repeated operation while rotating
Elbow joint	1.22112*	The bending of the thin section of the upper-elbow joint receptor under maximum arm load
Wrist joint	3.84*	Lateral loading and bending of the wrist in supporting the maximum end load during actuation.
Shoulder joint	1.97825*	The downward weight of the arm and maximum end load on the joint planar section where the upper arm propagates from and is supported
Shoulder socket joint	2.98*	Arm is under maximum load with muscle driving a maximum torque during abduction (to elevate the arm)
Shoulder rods	2.7	The downward bearing load of the shoulder pulley in driving the maximum torque specified for the arm at maximum load, equally resulting in torsional stress.
Double cardan joint	1.093	Total maximum torque of 59.1565 Nm applied to the short thin extension shaft during arm flexion/extension under maximum load

* Scaled by $\frac{1}{4}$ to accommodate lack of solid internal volume in 3D-printed components [38]

From the humanoid arm's CAD modelled design and simulated motion study, as well as its final assembled physical operation the following mechanical properties describe the arm's system.

Table 6.2: Overall arm mechanical properties

Mechanical Detail / Property	Value / Description
Critical stress region	Shoulder unit
Critical stress component	Double cardan joint extension shaft
Minimum factor of safety of critical component	1.093
Skeletal mass / g	962
Total Muscle mass / g	322
Muscle delivery tubes and auxiliary mass* / g	437
Total muscle mass situated on arm's skeleton / g	188
Total muscle mass situated on/within chest support / g	134
Total arm mass* / g	1721

* Includes mass of pump (280g); Excludes the mass of the battery and the support frame.

The frame itself does not constitute the arm as the arm is mountable on any designed frame of the humanoid to accommodate the shoulder support.

6.1.2 Actuation performance results summary

The muscle approximated parts, conclusively Load case can be identified as the most mechanically straining arm orientations and likewise would result in possible difficulty in driving motion under these orientations when loaded to a maximum.

Table 6.3: Arm operational performance

Mechanical Detail / Property	Value / Description
Maximum input pump power / W	12
Maximum power transmitted / W	6.7464
Estimated maximum efficiency without control unit	56.22%

Arm power-to-weight ratio / W/kg	3.92
Maximum arm reach / m	0.72

6.2 Discussions

Based on the assessed load cases in Table 3.8 and the least safe load means on the following primary parts (Table 6.1), conclusively load case 1(a, b, c) and 3(a, b, c) can be identified as the most mechanically straining arm orientations. The results show considerable reduced factor of safety when the arm is in full extension (forearm extended and shoulder extended) forward and/or elevated. These load cases would result in possible difficulty in driving motion under the given arm orientations when loaded to a maximum.

The computed power-to-weight ratio takes into account the housed miniature pump's mass as an addition to the arm's mass. However, in considering that such a miniature pump would be housed within the body of the humanoid or remain rested within the support/table, the maximum power-to-weight ratio can ignore the pump's mass. As such the humanoid arm designed has a final maximum power to weight ratio of 4.68175 W/kg.

The arm's low power efficiency in this application is likely due to the muscle's power consumption in resisting the elastic forces of its tubing, time used in pressurizing the entire muscle tube system and time used in inflating till sleeve contact before contraction. As such, the arm would display a better power output and efficiency in maintaining continuous, near constant velocity operation, as opposed driving load from rest through an acceleration. The incorporation of a control system to automatically regulate the pump with the coupled valve control unit would decrease the required running power of the pump motor due to the assisted pressure regulation and pressure hold, as such efficiency would increase.

The aforementioned results in Table 6.1-6.2 are herein discussed and compared against the project design goals and specification encompassed under the evaluation criteria (Table 3.2). Firstly, the Bill of Materials approximate a build cost of \$830 of which falls within the

low-cost design goal outlined for this product design for its intended manufacturing market elaborated in Chapter 1. With a specified F.O.S limit for the arm's safe operation and durability in the evaluation criteria, the project meets the desired range of 1-4 for all p primary components (Table 6.1) of which do not catastrophically fail under fatigue and/or static loading. The arm meets the expected workspace reach of the average human arm; however, its biomimetic accuracy could not be fully validated without a comprehensive control system to automate joint positioning.

The arm demonstrates an approximate linear relationship between force (load) and muscle contraction (strain) for small load ranges under constant pressure. Thus, for the need to accelerate an end load from one holding position to another based on the estimated forces in Table 3.14, an expected contraction value can relatively accurately be estimated under this experimental model. However, the muscles were not tested to their ultimate pressure specification in Table 3.16 under a 9kg load. These high force applications of the PAM have been theoretically and experimentally estimated to be feasible and a demonstrated FEM modelling [40] of the McKibben tubing offers better performance estimates of the muscle, and aids in eliminating the 4-20% deviation in Figure 5.6 and 5.7.

Chapter 7: Conclusion and Future Work

This chapter concludes this project and captures the resulting outcome of the modularized humanoid arm designed and implemented. Highlighted are the project's uniqueness and notable design features, encountered limitations and future works to improve the mechanical design and integrate a semi-automatic/automatic adaptive control system.

7.1 Conclusion

This project successfully introduces a new design to a humanoid arm to be powered by PAM. The design's uniqueness lies in the introduction of a double cardan joint, which is constant velocity joint, in the shoulder. This allows for the situating of the more than 66% of the shoulder muscles required for the arm's highest degree of freedom within the chest area of the humanoid body, consequently adding to the goal of weight reduction of the arm manoeuvrable part of the arm, and in turn, a power to weight ratio of 4.68175 W/kg. There is 2the arm's weight when more actuators are situated on the arm.

Additionally, the weight (skeletal, muscular and auxiliary) distribution of the arm results in up to 72% spread on and within the chest support and 28% decreasingly along the arm length from the shoulder support. This offers better stability for final integration into any humanoid robot.

The use of a miniature pressure-pump with muscle load design dimensioned and situated to only require a maximum driving pressure of 426.375 kPa, not only contributes to the high power-to-weight ratio of the arm but creates the arm as a complete modularized unit of which can remain mobile and operational without an attached-to humanoid or tether to an external compressor.

The use of a pre-existing cardan joint and centring ball joint in creating this double cardan joint is advised to ensure safer operation within the joint's stress limits, than the shaft

extension mechanism. Additionally, it would help eliminate any potential friction during arm elevation as the shaft contracts into or out of the joint.

Compared to existing solutions, the design goals met makes the arm notably cheaper and easier to reproduce and has made considerable strides in cutting down weight and leveraging the high power-to-weight ratios of the PAM. The humanoid arm with a near 5W/kg power-to-weight ratio and 2kg weight (without sensors) surpasses the competitive solutions within this lightweight category such as the Mitsubishi PA10 arm of weight 38kg and the KUKA lightweight arm of weight 14kg and power-to-weight ratio of 1W/kg [41].

7.2 Future Work

With a complete and mechanically tested modularized humanoid arm design, further development into the arm's automatic/semi-automatic control, increase in its wrist degree of freedom, joint improvement and mechanical advantage can be explored.

7.2.1 Proposed Control System

This subsection details a proposed design for the humanoid arm. Due to the hysteresis effect of the McKibben tubing muscles in either extending or contracting, and non-linear regions of for instance dead zone in which the inner tubing is not in contact with the sleeving from its relaxed state, there are broad variations in muscle performance across the selected and design muscles. To cater for these variations, a feedback control system must be utilized in order to read current muscle states and adjust pressure input to attain the set value. Additionally, during operation muscle heating from friction with the sleeving is a likely cause of performance deviation, thus predefined transfer functions and models may become inapplicable for not only other muscles but for the same muscle over continuous use.

With the mentioned difficulties, a Machine Learning control system is designed for an Arduino Microcontroller of which adapts and learns based on the muscle feedback the estimated muscle performance at every point in time and self-adjusts model parameters accordingly. The type of Machine Learning chosen to overcome these complexities is Reinforcement Learning (RL), as this is the applicable ML type for this control system in such a dynamic environment. Other ML types being supervised learning and unsupervised learning deal with labelling and clustering.

This black box approach to controls helps eliminate the complex steps of sensor data extraction, kinematic modelling, and the fluid dynamics of the pneumatic control as well other state space conversions.

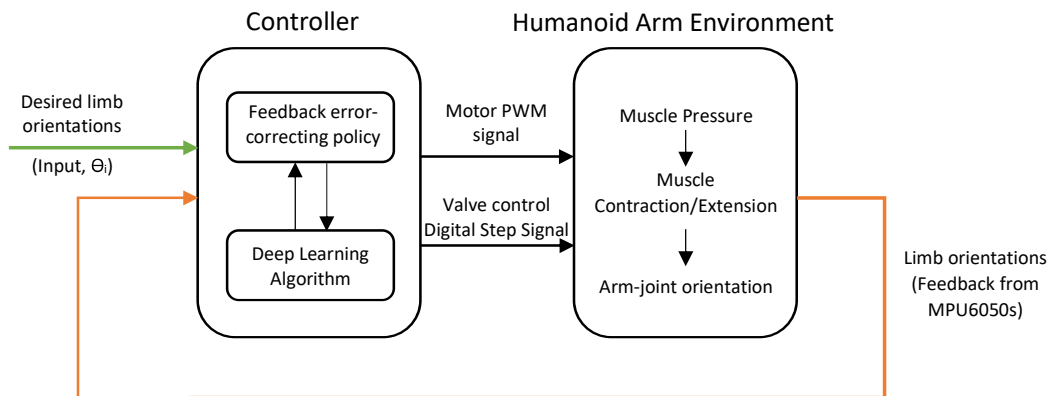


Figure 7.1: Proposed humanoid arm control system flow chart

With an efficient control system for the pressurization and depressurization of the muscles, the system efficiency can be calculated by observing the system electrical power input against the arm’s mechanical power output over the controlled operational time.

7.2.2 Muscle Optimization

Having proceeded to evaluate the muscles’ estimated performances and required force outputs, the effect of increasing the number of McKibben tubing constituting one muscle can be investigated to find a balance between muscle response against the muscle’s load per unit.

A larger number of tubing coupled together per muscle type results in a larger volume to pressurize, and in turn affects the muscle's response time for the same pump volumetric rate. Consequently, the increased number of McKibben tubing per muscle cluster would result in higher muscle rigidity during pressurization.

7.2.3 Joint improvements for mechanical advantage

With the chosen joint types, there are possibilities to increase the mechanical advantage of the pulleyed knuckle joint of the elbow and wrist. Pulley systems in which the driving muscle loops over a multi-pulley unit instead of a single one would reduce the required force needed by the muscle to attain the torque output at the joint.

Lastly, the double cardan joint designed acts as a constant velocity joint with a degree of freedom of its rotational axis, there are other constant velocity joints that offer merits or demerits to the design; however, some designs are proprietary. Further advancement of the project can explore the substitution of a higher mechanically advantaged constant velocity joint for this design purpose.

References

- [1] C. Laschi and M. Cianchetti, “Soft Robotics: New Perspectives for Robot Bodyware and Control,” *Front. Bioeng. Biotechnol.*, vol. 2, 2014, doi: 10.3389/fbioe.2014.00003.
- [2] M. Slamani, A. Nubiola, and I. Bonev, “Modeling and assessment of the backlash error of an industrial robot,” *Robotica*, vol. 30, pp. 1167–1175, Dec. 2012, doi: 10.1017/S0263574711001287.
- [3] N. El-Atab *et al.*, “Soft Actuators for Soft Robotic Applications: A Review,” *Advanced Intelligent Systems*, vol. n/a, no. n/a, p. 2000128, doi: 10.1002/aisy.202000128.
- [4] V. Cacucciolo, H. Nabae, K. Suzumori, and H. Shea, “Electrically-Driven Soft Fluidic Actuators Combining Stretchable Pumps With Thin McKibben Muscles,” *Front. Robot. AI*, vol. 6, 2020, doi: 10.3389/frobt.2019.00146.
- [5] T. Gailliard, “What Robots Are Used Today?,” *Sciencing*, Jun. 27, 2018. <https://sciencing.com/what-robots-are-used-today-12745877.html> (accessed Oct. 06, 2020).
- [6] “Humanoid Robot Market, by Product, Application, Regional Analysis: Global Opportunity Analysis and Industry Forecast, 2019–2026,” SE : Emerging and Next Generation Technologies, RA00110, Apr. 2020. [Online]. Available: <https://www.researchdive.com/110/humanoid-robot-market>.
- [7] L. Novitske, “The AI Invasion is Coming to Africa (and It’s a Good Thing) (SSIR),” *Stanford Social Innovation Review*, Feb. 12, 2018.
- [8] T. Bock, T. Linner, and W. Ike, “Exoskeleton and Humanoid Robotic Technology in Construction and Built Environment,” in *The Future of Humanoid Robots - Research and Applications*, R. Zaier, Ed. InTech, 2012.
- [9] A. S. Gorgey, “Robotic exoskeletons: The current pros and cons,” *World J Orthop*, vol. 9, no. 9, pp. 112–119, Sep. 2018, doi: 10.5312/wjo.v9.i9.112.

- [10] L. Azas, "Robo competition to help enhance knowledge in robotics, AI," GhanaWeb, Nov. 21, 2019. <https://www.ghanaweb.com/GhanaHomePage/NewsArchive/Robo-competition-to-help-enhance-knowledge-in-robotics-AI-801116> (accessed Oct. 06, 2020).
- [11] Digital Times Africa, "Ghanaian Inventor Designs A Humanoid Prototype," Medium, Jul. 03, 2020. https://medium.com/@digitaltimes_2020/ghanaian-inventor-designs-a-humanoid-prototype-6ce2e413f07e (accessed Oct. 06, 2020).
- [12] E. Howell and 2019, "NASA Is Developing 'Soft Robots' to Help Explore Other Worlds," Space.com, May 08, 2019.
- [13] C. Kenny, "Automation and AI: Implications for African Development Prospects?," Center For Global Development, Oct. 2019, Accessed: Oct. 06, 2020. [Online]. Available: <https://www.cgdev.org/publication/automation-and-ai-implications-african-development-prospects>.
- [14] "Soft Robotics Market - Growth, Trends, and Forecast (2020 - 2025)," Modor Intelligence, Hyderabad, India, May 2020. Accessed: Oct. 06, 2020. [Online]. Available: <https://www.researchandmarkets.com/reports/4534396/soft-robotics-market-growth-trends-and>.
- [15] "Soft Robotics Market, Share & Growth | Analysis & Trend, 2020-2027," DataM Intelligence. Accessed: Oct. 06, 2020. [Online]. Available: <https://www.datamintelligence.com/research-report/soft-robotics-market>.
- [16] B. Pierce and G. Cheng, "Herbert: Design and Realization of a Full-Sized Anthropometrically Correct Humanoid Robot," *Front. Robot. AI*, vol. 2, 2015, doi: 10.3389/frobt.2015.00014.
- [17] S. Mick et al., "Reachy, a 3D-Printed Human-Like Robotic Arm as a Testbed for Human-Robot Control Strategies," *Front. Neurobot.*, vol. 13, 2019, doi: 10.3389/fnbot.2019.00065.

- [18] S. Hunt, "A Guide to Manual Handling and Lifting Techniques," Workplace Safety Advice, Aug. 22, 2020. <http://www.workplacesafetyadvice.co.uk/guide-manual-handling-lifting-techniques.html> (accessed Oct. 20, 2020).
- [19] H. Shen, S. Rojas, E. Molina, F. Moxo Galicia, and N. Li, "Development and Analysis of Robotic Arms for Humanoid Melo," in Volume 4A: Dynamics, Vibration, and Control, Pittsburgh, Pennsylvania, USA, Nov. 2018, p. V04AT06A030, doi: 10.1115/IMECE2018-87987.
- [20] P. Voosen, "Could Battery Advances Mean a Better Robot? - Scientific American," Scientific American, Aug. 26, 2009.
- [21] J. K. Paik, B. H. Shin, Y. Bang, and Y.-B. Shim, "Development of an Anthropomorphic Robotic Arm and Hand for Interactive Humanoids," Journal of Bionic Engineering, vol. 9, no. 2, pp. 133–142, Jun. 2012, doi: 10.1016/S1672-6529(11)60107-8.
- [22] Y. Moon, N. Y. Ko, and Y. Bae, "The Design of Humanoid Robot Arm Based on Morphological and Neurological Analysis of Human Arm," Humanoid Robots, Jan. 2009, doi: 10.5772/6730.
- [23] D. Tanaka, D. Kamo, M. Maehara, and T. Nakamura, "Development of two types of 2-DOF wrist joint driven by pneumatic artificial muscles," in 2013 IEEE International Conference on Mechatronics (ICM), Vicenza, Feb. 2013, pp. 471–476, doi: 10.1109/ICMECH.2013.6518582.
- [24] E. Elisabeth, "Basics of Rotary Encoders: Overview and New Technologies | Machine Design," MachineDesign, May 07, 2014. <https://www.machinedesign.com/automation-iiot/sensors/article/21831757/basics-of-rotary-encoders-overview-and-new-technologies> (accessed Apr. 27, 2021).
- [25] J. Wu, T. Zhou, B. Yuan, and L. Wang, "Absolute angular encoder based on optical diffraction," vol. 9623, p. 962304, Aug. 2015, doi: 10.1117/12.2191494.

- [26] L. Eitel, “POSITAL Motor Feedback Kit Encoders — now with open-source BiSS interface,” Motion Control Tips, Jan. 25, 2018. <https://www.motioncontroltips.com/posital-motor-feedback-kit-encoders-now-open-source-biss-interface/> (accessed Apr. 27, 2021).
- [27] W. Felt and C. D. Remy, “Smart braid: Air muscles that measure force and displacement,” in 2014 IEEE/RSJ International Conference on Intelligent Robots and Systems, Chicago, IL, USA, Sep. 2014, pp. 2821–2826, doi: 10.1109/IROS.2014.6942949.
- [28] D. Caldwell, G. Medrano-Cerda, and M. Goodwin, “Control of Pneumatic Muscle Actuators,” Control Systems, IEEE, vol. 15, pp. 40–48, Mar. 1995, doi: 10.1109/37.341863.
- [29] V. Cacucciolo, H. Nabee, K. Suzumori, and H. Shea, “Electrically-Driven Soft Fluidic Actuators Combining Stretchable Pumps With Thin McKibben Muscles,” Front. Robot. AI, vol. 6, 2020, doi: 10.3389/frobt.2019.00146.
- [30] R. Niiyama, C. Rognon, and Y. Kuniyoshi, “Printable pneumatic artificial muscles for anatomy-based humanoid robots,” in 2015 IEEE-RAS 15th International Conference on Humanoid Robots (Humanoids), Seoul, South Korea, Nov. 2015, pp. 401–406, doi: 10.1109/HUMANOIDS.2015.7363565.
- [31] C. Dube and J. Tapson, “Kinematics design and human motion transfer for a humanoid service robot arm,” undefined, 2009, Accessed: Apr. 27, 2021. [Online]. Available: </paper/Kinematics-design-and-human-motion-transfer-for-a-Dube-Tapson/469bbe12dd7bb639659999ea37d25604755e23e7>.
- [32] A. Gomes, J. Mendes, and J. Tavares, “Sabioteñist – Sistema de Análise Biomecânica de Tenista,” Feb. 2015, doi: 10.13140/2.1.3448.4004.
- [33] D. Shah, Y. Wu, A. Scalzo, G. Metta, and A. Parmiggiani, “A Comparison of Robot Wrist Implementations for the iCub Humanoid †,” Robotics, vol. 8, no. 1, Art. no. 1, Mar. 2019, doi: 10.3390/robotics8010011.

- [34] C. Chou and B. Hannaford, "rement and ding of McKibben Pneumatic Artificial Muscles," undefined, 1996, Accessed: Apr. 27, 2021. [Online]. Available: /paper/rement-and-ding-of-McKibben-Pneumatic-Artificial-Chou-Hannaford/639d955b16997d4768e49b337c4177673a1bbc0e.
- [35] A. Al-Ibadi, S. Nefti-Meziani, and S. Davis, "Design, implementation and modelling of the single and multiple extensor pneumatic muscle actuators," *Systems Science & Control Engineering*, vol. 6, no. 1, pp. 80–89, Jan. 2018, doi: 10.1080/21642583.2018.1451787.
- [36] Tondu, B., and Lopez, P. (2000). Modeling and control of McKibben artificial muscle robot actuators. *IEEE Control Systems*, 20, 15–38. doi: 10.1109/37.833638
- [37] R. Budynas, *Shigley's Mechanical Engineering Design*, 10th ed. McGraw-Hill Higher Education, 2014.
- [38] "Optimizing Strength of 3D Printed Parts," 3DPros. <https://www.3d-pros.com/optimizing-strength-of-3d-printed-parts> (accessed Apr. 27, 2021).
- [39] C. E. Cooney, "Double Cardan Constant Velocity Universal Joint," *SAE Transactions*, vol. 83, pp. 2489–2497, 1974.
- [40] Q. Tu, Y. Wang, D. Yue, and F. A. Dwomoh, "Analysis on the Impact Factors for the Pulling Force of the McKibben Pneumatic Artificial Muscle by a FEM Model," *Journal of Robotics*, vol. 2020, p. e4681796, Jan. 2020, doi: 10.1155/2020/4681796.
- [41] G. Hirzinger and A. Albu-Schaeffer, "Light-weight robots," *Scholarpedia*, vol. 3, no. 4, p. 3889, 2008, doi: 10.4249/scholarpedia.3889.

Appendix

Appendix A

Fatigue (S-N) curves

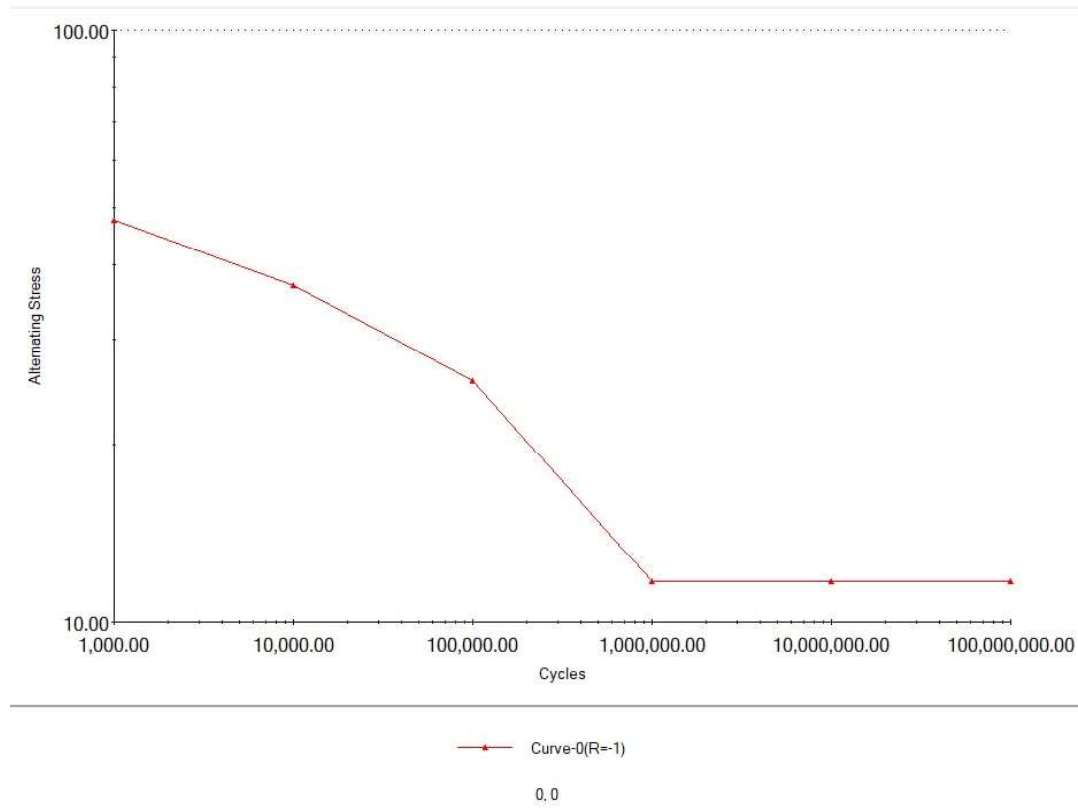


Figure A.1: S-N generated curve for ABS material

Appendix B

Table B.1: Moving mass and torque at joints

Joint type	Moving mass, m / kg	Loaded torque, T / Nmm
Wrist joint flexion/extension	9.06422	1500.93
Elbow joint flexion/extension	9.13172	25811.8
Upper arm shoulder rotation	9.13172	27014.9
Shoulder joint flexion/extension	9.19855	59156.5
Shoulder joint abduction/adduction	9.19855	51969.5

Appendix C

Table C.1 Small Muscle Experimental Load-Contraction Data at 50 kPa

Muscle Pressure / kPa	Spring Force / N	Muscle Contraction / mm						
		T1	T2	T3	T4	T5	T6	T7
50	6	44	44	45	43	45	44	42
50	8	26	27	32	29	27	25	29
50	10	21	19	21	21	21	20	19
50	12	4	5	5	5	4	5	3

Table C.2 Small Muscle Theoretical Load-Contraction Data at 50 kPa

Muscle Pressure / kPa	Spring Force / N	Muscle Contraction / mm
50	6	57.518
50	8	41.039
50	10	24.561
50	12	8.082

Table C.3 Large Muscle Experimental Load-Contraction Data at 50kPa

Muscle Pressure / kPa	Spring Force / N	Muscle Contraction / mm						
		T1	T2	T3	T4	T5	T6	T7
50	6	98	97	100	105	97	97	97
50	8	95	95	95	95	98	96	95
50	10	93	93	95	94	94	95	95
50	12	92	90	90	93	92	92	93

Table C.4 Large Muscle Theoretical Load-Contraction Data at 50 kPa

Muscle Pressure / kPa	Spring Force / N	Muscle Contraction / mm
50	6	101.461
50	8	99.63
50	10	97.799
50	12	95.968

Valve Specifications

Valve Specifications

Model

Type	Type of actuation	Model	Flow-rate characteristics						Response time [msec]	Weight [g]	
			1→4/2 (P→A/B)			4/2→5/3 (A/B→R1/R2)					
			C [dm ³ /[s·bar]]	b	Cv	C [dm ³ /[s·bar]]	b	Cv			
Body Ported	Single Unit Page 7	2-position Single	S0716	0.62	0.44	0.18	0.60	0.41	0.17	22 or less	39
		2-position Double	S0726	0.62	0.44	0.18	0.60	0.41	0.17	10 or less	47
		3-pos. 3-pos. closed center	S0736	0.54	0.37	0.15	0.50	0.38	0.14	45 or less	47
		4-pos. 3-pos. Dual 3-port valve	S0736 A C	0.58	0.39	0.16	0.67	0.37	0.18	25 or less	49
	Manifold Bar Base Page 10	2-position Single	S0712	0.51	0.40	0.15	0.64	0.33	0.15	22 or less	34
		2-position Double	S0722	0.51	0.40	0.15	0.64	0.33	0.15	10 or less	42
3-pos. 3-pos. closed center		S0732	0.54	0.37	0.10	0.46	0.38	0.08	45 or less	42	
4-pos. 3-pos. Dual 3-port valve		S0732 A C	0.57	0.39	0.15	0.55	0.37	0.15	25 or less	44	
Base Mounted	Single Unit Page 12	2-position Single	S0715	0.39	0.39	0.11	0.37	0.39	0.10	12 or less	28
		2-position Double	S0725	0.39	0.39	0.11	0.37	0.39	0.10	10 or less	36
	Manifold Bar Base Page 15	3-pos. 3-pos. closed center	S0735	0.29	0.29	0.07	0.26	0.21	0.06	28 or less	38
		4-pos. 3-pos. Dual 3-port valve	S0735 A C	0.34	0.34	0.09	0.33	0.33	0.08	12 or less	36

Note 1) Values for cylinder port fitting port size C4. The flow rate of a body ported single valve is the SUP and EXH port C4 value.
 Note 2) Based on JIS B 8375-1993 (Supply pressure: 0.5 MPa, with indicator light and surge voltage suppressor, clean air. This will change depending on pressure and air quality.) The value when ON for the double type.
 Note 3) The weight of a single unit of the valve includes a built-in EXH port silencer.
 Note 4) The flow rate of the body ported product with an external pilot decreases by 10%.
 Note 5) The flow rate of the body ported product with a built-in silencer decreases by 30%.

Specifications

Valve specifications	Valve construction	Rubber seal
	Fluid	Air
	Maximum operating pressure	0.7 MPa
	Minimum operating pressure	0.2 MPa
	Ambient and fluid temperature	-10 to 50°C <small>Note 1)</small>
	Maximum operating cycle	5 Hz
	Pilot valve exhaust method	Individual exhaust
	Pilot valve manual override	Push type
	Lubrication	Not required
	Impact/Vibration resistance <small>Note 2)</small>	30/100 m/s ²
	Enclosure	IP40
Electrical specifications	Noise reduction (Built-in silencer)	20 dB(A) <small>Note 3)</small>
	Coil rated voltage	24 VDC
	Allowable voltage fluctuation	±10% of rated voltage
	Coil insulation type	Class B or equivalent
	Power consumption (Current) 24 VDC	DC 0.35 W (15 mA)

<http://ca01.smcworld.com/catalog/New-products-en/mpv/es11-109-s0700/data/es11-109-s0700.pdf>

Figure D.1: Specifications for Sub-miniature pilot 5/3-way solenoid valve

Appendix E

Standard Specifications:

Valve Type: 2-Way Normally Closed (proportional)

Media: Air & Inert Gases

Operating Pressure: See charts

Voltages: 12 or 24 VDC

Orifice Diameters: 1/16" or 3/32"

Coil Type: 9 Watt– Class "F" 155°C with 1/4" Spades

Body: Stainless Steel

Port Size: 1/8" NPT

Seal Material: Buna N

Temperature Range: Normal 40°F to 70°F
(contact factory for settings outside this range)

Maximum Hysteresis*: 15%

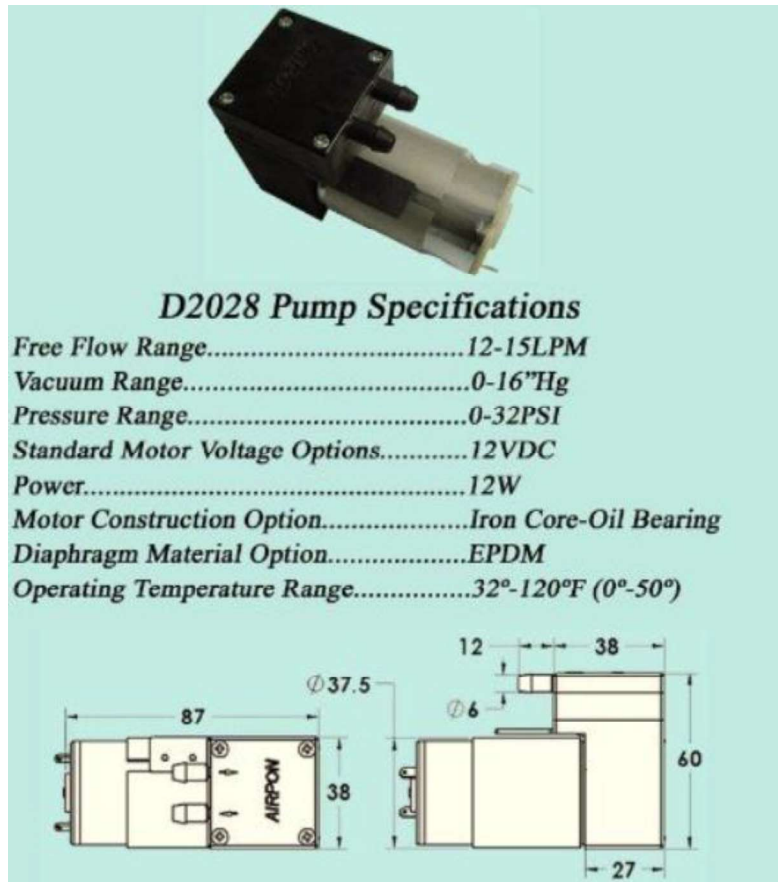
**Hysteresis - If an alternating magnetic field is applied to the material, its magnetization will trace out a loop called a hysteresis loop. The lack of retracability of the magnetization curve is the property called hysteresis and it is related to the existence of magnetic domains in the material.*



https://www.solenoidsolutionsinc.com/images/pdfs/ProportionalValveBrochure_216.pdf

Figure E.1: Specifications for Wattmizer Proportional 2 Way Normally Closed Valves

Appendix F



<https://www.sparkfun.com/datasheets/Robotics/Other/spec%20sheet.jpeg>

Figure F.1: Datasheet for the Airpo D2028B Miniature-Pressure Pumps

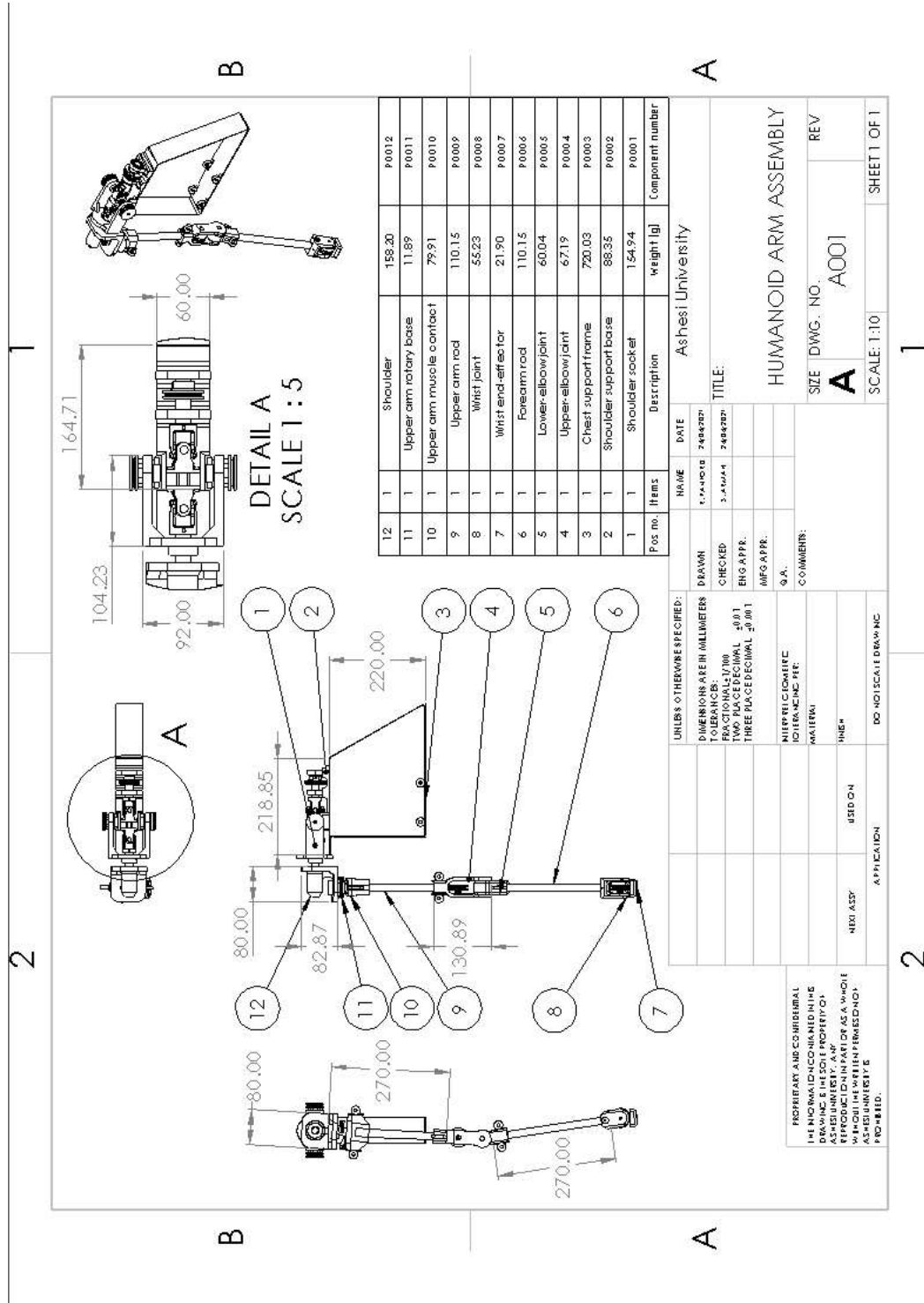


Figure G.1: Assembly drawing